Anoxic corrosion of carbon steel in high pH cementitious media and high temperature conditions: New insights on the formation of (Fe,Al)Si-hydrogarnet corrosion product

Jules Goethals, Laurent de Windt, Georges Dan Miron, Charles Wittebroodt, Abdesselam Abdelouas

Corrosion Science 237 (2024) 112318

Contents lists available at ScienceDirect

Corrosion Science

journal homepage: www.elsevier.com/locate/corsci

Anoxic corrosion of carbon steel in high pH cementitious media and high temperature conditions: New insights on the formation of (Fe,Al) Si-hydrogarnet corrosion product

Jules Goethals [a,*], Laurent De Windt [b], Georges Dan Miron [c], Charles Wittebroodt [d], Abdesselam Abdelouas [a]

[a] Laboratoire Subatech, UMR 6457, 4 Rue Alfred Kastler, La Chantrerie CS 20722, Nantes CEDEX 3 44307, France
[b] Mines Paris, PSL University, Centre for Geosciences and Geoengineering, 35 Rue St-Honoré, Fontainebleau 77300, France
[c] Paul Scherrer Institute, Laboratory for Waste Management, Forschungsstrasse 111, Villigen PSI 5232, Switzerland
[d] Institut de Radioprotection et de Sûreté Nucléaire (IRSN)/LETIS, 31 Avenue de la Division Leclercq, BP 17, Fontenay-aux-Roses Cedex 92262, France

ARTICLE INFO

Keywords:
Carbon steel
Supercontainer design
Hydrogarnet
Nuclear waste disposal
Anoxic conditions
HYTEC

ABSTRACT

The corrosion of carbon steel in alkaline anaerobic conditions and high temperature (80°C) was studied through mock-up tests representative of imperfect contact between steel and cementitious material. The evolution of the whole system, including cement mineralogy, reservoir solution chemistry, corrosion product and rate, was followed over one year. SEM-EDX and XRD analyses indicated that the corrosion product layer was mostly constituted of (Fe,Al)Si-Hydrogarnet ((Fe,Al)Si-HG) and that its densification progressively inhibited corrosion. Thermodynamic and reactive transport modelling helped to better constrain the chemical and temperature conditions of (Fe,Al)Si-HG formation.

1. Introduction

From the 1950s, the deep geological repository (DGR) has been internationally considered as the best option for the management of nuclear waste with high level of radioactivity (denoted HLW) [1]. The strategies to allow safe disposal of HLW for hundreds of thousands of years may vary according to the different national geological context and the distinct rules and regulations in effect. But all strategies rely on the multi-barrier concept, globally made of a waste package, a buffer material and a host rock [2,3]. Cement-based materials are widely used as buffers. For instance, regarding the Belgian and Dutch envisioned DGR design [4], the HLW waste packages consist of stainless-steel canisters, containing the nuclear glass, encapsulated into low carbon steel overpack. In these concepts, the waste packages will be emplaced in a 700 mm thick CEM I concrete buffer encased in a steel liner, referred as the *supercontainer* design [4]. The Hungarian DGR design also relies on low carbon-steel containers containing the HLW encased in a prefabricated cylindrical CEM II concrete buffer material [5,6]. The role of such thick concrete buffer is to passivate low carbon steel by highly alkaline pH conditions. After the repository closure, O_2 from the air will be rapidly consumed [7] and high temperature (80°C) will be reached due to heat production by HLW radioactive decay [8]. In the long term, the cementitious buffer material, as well as its porewater solution, will evolve, mainly leading to the decrease of the pH of this latter [9].

With this respect, the corrosion of carbon steel in anoxic conditions has been investigated in the presence or absence of cementitious materials, at various temperatures, relative moisture contents and pH values (e.g. [10–16]). In most studies, the corrosion was generalized, even though the likelihood of pit initiation, while low, may not be negligible [17,18]. The corrosion rate of steel in such conditions decreased with time, down to values comprised between 1 μm/year to 0.1 nm/year, depending on the previously mentioned parameters as well as on the method to measure such low corrosion rates ([19]). The measured low corrosion rates were usually related to the formation of a passivating film at the surface of the steel (e.g. [20,21]). In some studies, an important effort was devoted to the identification of the steel corrosion products. Such studies mostly revealed that hematite (α-Fe_2O_3), lepidocrocite (γ-FeO(OH)), goethite (α-FeOOH), maghemite (γ-Fe_2O_3) and magnetite (Fe_3O_4) were the main corrosion products [6,14,15,22,23]. Magnetite was generally the dominant corrosion product in anaerobic conditions.

However, it was recently shown that Fe (hydr)oxides would not be

* Corresponding author.
E-mail address: jules.goethals@cea.fr (J. Goethals).

https://doi.org/10.1016/j.corsci.2024.112318
Received 16 May 2024; Received in revised form 22 July 2024; Accepted 23 July 2024
Available online 23 July 2024

the most thermodynamically stable phases in a cementitious environment and that (Fe,Al)Si-HG of the following composition $Ca_3(Al_{(1-x)}Fe_x)_2(SiO_4)_y(OH)_{4(3-y)}$ could rather form instead [24,25]. On the one hand, this phase can arise from the hydration of Fe-bearing cement clinker and additives and on the other hand, carbon steel can be a Fe source to produce such phase [25]. To the best of our knowledge, only one recent experimental study evidenced the formation of such (Fe,Al)Si-HG phase as a carbon steel corrosion product in the above mentioned conditions [26]. This previous work showed that a nanometric magnetite layer formed in a first stage until the ingress of elements coming from the cement (i.e., Ca, Si) favored the precipitation of (Fe,Al)Si-HG. However, a lot of questions remain regarding the parameters controlling the precipitation of such (Fe,Al)Si-HG phase against magnetite, and of the role of this phase on the long-term corrosion rate of carbon steel. Moreover, the use of low carbon-steel component presenting defective surfaces (e.g., presence of mill scale layer, rough surface) in real repository systems can have an impact on the corrosion mechanism and/or on the associated corrosion rate.

In the present study, the corrosion of carbon steel samples either embedded in a hydrated CEM I paste or immersed in a CEM I reservoir solution was investigated through laboratory experiments performed at 80 °C in the framework of the BACUCE project [24,27]. The impact of the initial steel surface condition (i.e., presence of mill-scale layer, rough or polished surface) on corrosion mechanisms was also studied. The time-dependent evolutions of (i) cementitious reservoir solution, (ii) cement mineralogy and (iii) carbon steel corrosion were investigated together to better apprehend the anoxic corrosion of low carbon steel at elevated temperature in cementitious media. The characterization of the samples by SEM-EDX and XRD together with geochemical modelling allowed a better understanding of the whole system evolution and identification of the parameters that promote (Fe,Al)Si-HG formation.

2. Materials and methods

2.1. Steel, cement and reservoir solution

2.1.1. Low carbon steel

Fig. 1-a gives the composition of the TU37b (A37) steel that was chosen for the BACUCE experiments due to its chemical similarity with the alloy of the steel casing (API 5 L X65 steel) selected in the French design for HLW geologic disposal. The mean composition of this steel was determined from 10 measurements made by optical spectrometry with a SPECTRO MAXx Ametek© (Fig. 1-a). This low carbon steel exhibits a ferrite-pearlite layered structure (Fig. 1-a). Its external mill scale layer has a heterogeneous microstructure and presents "indentations" of several tens of micrometres (Fig. 1-b). This mill scale layer is enriched in Na, P, O, Zn and Fe (Fig. 1-b) and the oxide layer is primarily made of magnetite [27]. The enrichment of Si observed in Fig. 1-b is linked to the presence of a gap between the resin and the steel where SiC polishing grains were trapped.

2.1.2. Hydrated ordinary Portland-cement

An ordinary Portland cement (CEM I, 52.5) from Val d'Azergues (Lafarges, France) was employed for this study and its composition is given in Table 1.

The hydrated cement paste (HCP) was produced using a water to cement ratio (W/C) of 0.42. After 28 days of hydration at ambient temperature, the mineralogical composition of the HCP was examined. The results are in close agreement with the one obtained in previous studies [28,29]. Briefly, the XRD pattern collected on a disked sample (see Section 2.5.2 for the method) revealed the presence of portlandite, C-S-H, ettringite, hemicarboaluminate, monocarboaluminate, calcite and (Fe,Al)Si-HG as the main hydration products (Fig. SI-1). For the latter phase, the formulation $Ca_3(Al_{(1-x)}Fe_x)_2(SiO_4)_y(OH)_{4(3-y)}$ can be given but the exact composition is not known from the XRD data. When observed by XRD in cementitious material, this phase can be considered as Si-katoite $Ca_3Al_2(SiO_4)_y(OH)_{4(3-y)}$ [28,30] but a Al/Fe ratio of

Table 1
Chemical composition of CEM I from Val d'Azergues and mineralogical analysis provided by the manufacturer.

Chemical analyses (g/100 g)	
CaO	64.6
SiO_2	20.7
Al_2O_3	3.2
Fe_2O_3	4.5
CaO(free)	1.8
MgO	0.6
K_2O	0.6
Na_2O	0.1
CO_2	1.1
SO_3	2.8
Mineralogical analyses (g/100 g)	
Alite (C_3S)	65.3
Belite (C_2S)	13.5
Aluminate (C_3A)	0.9
Ferrite (C_4AF)	13.5
Total clinker	93.2
Gypsum	3.9
Filler	2.9

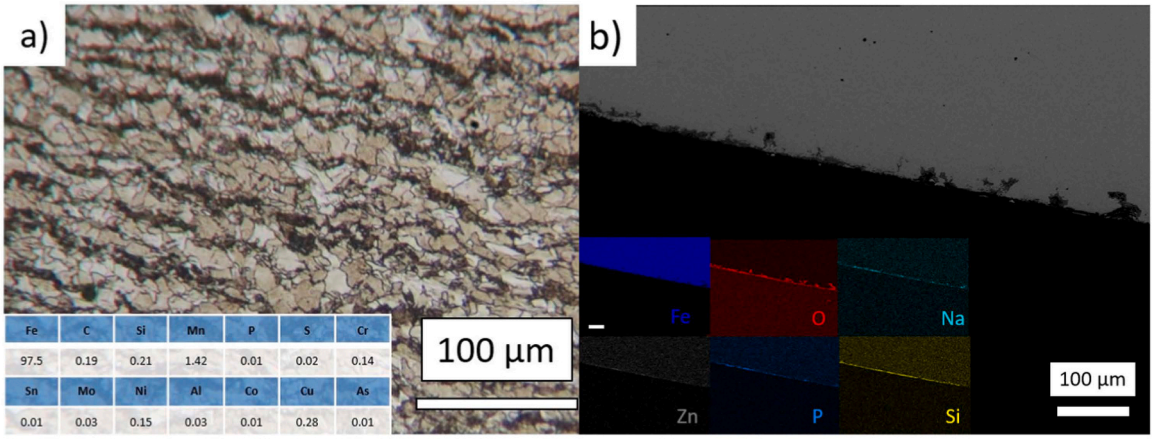

Fig. 1. (a) Microstructure parallel to the rolling direction and composition of the TU37b steel measured by optical emission spectrometry; (b) SEM-EDX mapping of the external mill-scale layer of the Tu37b steel. The microstructure of the steel was revealed after polishing the steel surface down to 0.05 µm with silicon colloids following chemical etching with a 2 % HNO_3 Nital solution.

approximately 0.5 was measured by EDX for this phase in an old mortar [31]. Although scarcely observed in cement paste, this phase is thermodynamically predicted in HCP [25,30,32,33]. The presence of residual C_3S, C_2S, C_4AF as the main unreacted cement (UC) phases is also observed. The amount of portlandite (17 vol%) and calcite (2 vol%) were determined by themogravimetric (TG) analyses and the combined amount of C_2S/C_3S (8 ± 1 vol%) and C_4AF (3 ± 0.5 vol%) were determined by SEM grey level analyses. The porosity (35.7 ± 0.3 %) was obtained from water content measurements performed on 3 samples.

2.1.3. Synthetic reservoir solution

A hyperalkaline solution that mimics the so called "young cement porewater" solution was prepared by mixing appropriate amount of NaOH (pellets, 98 % purity, Fluka®), KOH (pellet, 98 % purity, Fluka®) and $Ca(OH)_2$ (99 % purity, Alfa Aesar®) in vacuum degassed MilliQ® water (18.2 MΩ.cm at 25 °C). The pH of this solution was measured at 20 °C (13.6 ± 0.1) and 80°C (12.1 ± 0.1) and the chemical composition was analysed after fifteen days of heating at 80°C (Table 2).

2.2. Experimental set-up

Two types of experiment were designed to study both the corrosion of steel, either in direct contact with HCP or immersed in CEM. Experiment 1-R (EXP 1-R) was dedicated to (i) study the corrosion of steel, either in direct contact with HCP, or in the presence of an imperfect contact, (ii) evaluate the effect of the initial steel surface condition (i.e., presence of mill-scale layer, rough or polished surface) on the corrosion rates and (iii) assess the solution composition and pH change with time. For this purpose, TU37b steel rods of 3.1×1.5×1.0 cm^3 were cut from a TU37b tube section. Of the six exposed surfaces of the rod, three were ground with 180 SiC grit paper (top, bottom and left sides), one was polished with diamond paste down to 3 μm and on the two other sides, the pristine mill scale layers were preserved (Fig. 2-b). HCP was prepared in an anoxic glove box by mixing the ordinary Portland cement (OPC) with degassed water (Water/Cement ratio = 0.42) and directly poured in the PTFE reactors so that half of the rod height was embedded in CEM I (Fig. 2-a and Fig. 2-b). After pouring, HCP was let to harden during 28 days in the closed PTFE reactors prior to their partial filling with the CEM I reservoir solution (Table 2). Despite the fact that the samples were prepared in an anoxic glove box, one can note that oxic corrosion processes impacted to some extent the unembedded steel surfaces during the initial phase of HCP paste hardening. As it was not possible to retrieve the steel rods from the HCP, grinding and polishing operations were repeated in anoxic glove box to remove the corrosion products formed on the unembedded part of the metallic samples. In addition, one sample was sacrificed to check the extent of corrosion processes impacting the embedded part of the metallic rod. Examination of the steel surface under optical microscope revealed that damage causes by corrosion were very limited. Once HCP setting phase was achieved, at ambient conditions, and after a last grinding and polishing operation, the six remaining 1-R PTFE reactors were filled with 18 mL of reservoir solution (Table 2) and transferred in an oven under argon atmosphere at 80°C.

Experiment 2-C (EXP 2-C) was dedicated to (i) investigate the corrosion of steel in the presence of the CEM I, but without direct contact between the two materials and (ii) follow the mineralogical evolution of the CEM I with time at 80°C. For this purpose, TU37b steel coupons of 1.0×1.5×0.2 cm^3 were cut so that the 1.0×1.5 cm^2 surface area was perpendicular to the rolling direction of a TU37b tube section. CEM I disks of (ϕ) 27 mm × (h) 2 mm were cut from CEM I cylinders prepared in a similar manner as for EXP 1-R (Fig. 2-c). After 28 days, at ambient condition, the disks were put at the bottom of PTFE reactors, and the steel coupons were inserted in a PTFE basket located above the disks, in order to avoid any contact of steel with the cement disks nor the PTFE reactor. The six 2-C PTFE reactors were then filled with 6.6 mL of the CEM I reservoir solution and put in an oven under argon atmosphere at 80°C. The dimensions of both 1-R and 2-C experimental systems were set to obtain cement surface to CEM I reservoir solution volume ratio and exposed steel surface to reservoir solution ratio values close to the ones existing for an *in situ* experiment of the BACUCE project (2.24 and 0.66, respectively). Samples from each experiment were periodically retrieved and characterized following the different methods presented in the next sections.

2.3. Solid sample preparation for micro characterization

The steel-HCP assembly from EXP 1-R was first transferred in an anoxic glove box and immersed in deaerated ethanol (99 %) for 4 h to stop corrosion. Then, the samples were dried at least 12 h inside the glove box using silica gel prior to be embedded in Struers© Epoxy resin. After this, slices of both HCP covered and uncovered steel sample parts were cut perpendicularly to the rod axis with a diamond wire saw and ethanol as lubricant. The samples were then polished with SiC grit paper and diamond paste, down to 1 μm. As the sample preparation was performed in aerated conditions, the polishing operation was done just before the analyses to reduce the impact of sample preparation on oxidation of the samples and the latter were transported to the different analysing facilities in an argon-containing sealed box.

2.4. Solution analyses

Reservoir solution from EXP 1-R was sampled at different time and analysed to monitor its chemical evolution with time. Periodically, reactors were retrieved from the oven, put in an in-house isothermal container to maintain the temperature at 80°C and transferred in an anoxic glove box. For pH measurements, a fraction of the solution was transferred in a thermostated bath with temperature set at 80°C and measurements were made with a pH electrode (Mettler-Toledo) freshly calibrated with IUPAC pH buffer (9.18 and 12.46 at 25°C). The other fraction of the solutions was filtered with 0.2 μm PTFE Millipore© membrane filter and rapidly diluted in an adapted medium for further analyses (i.e., 2 % mass.HNO3 or MilliQ water) to avoid precipitation after cooling. Major cations (Na^+, K^+, Ca^{2+}, Mg^{2+}, Sr^{2+}) and anions (Cl^-, F^-, SO_4^{2-}, NO_3^-) were analysed by means of ionic chromatography with a Metrohm 850 Professional IC. ICP-MS analyses of Fe, Al and Si were carried out with a Q (quadrupole)-ICP-153 MS (Thermo Scientific X Series 2).

2.5. Solid sample characterization methods

2.5.1. Scanning electron microscopy

Scanning electron microscopy (SEM) coupled with energy dispersive X-ray spectroscopy (EDX) was used to conduct analyses on the embedded polished samples coming from EXP 1-R as well as on one steel coupon coming from EXP 2-C (sampled after 28 days of interaction) dedicated to metallic surface analyses and initially formed corrosion products identification. SEM-EDX analyses were performed with a JEOL 5800 LV microscope operating at 15 kV and 0.5 nA. Acquisition time of the EDX measurements was fixed to 60 s. Due to the potential presence of non-oxide minerals in the corrosion product layer, oxygen content

Table 2
Composition of the synthetic reservoir solution measured after fifteen days of heating at 80°C. The total concentrations are given in mol/L.

Na^+	K^+	Ca^{2+}	SO_4^{2-}	Cl^-	Si	Fe	Al^{3+}
5.2×10^{-2}	2.4×10^{-1}	1.5×10^{-3}	2.0×10^{-5}	$>3.7\times10^{-4}$	2.5×10^{-5}	1.8×10^{-5}	1.9×10^{-6}

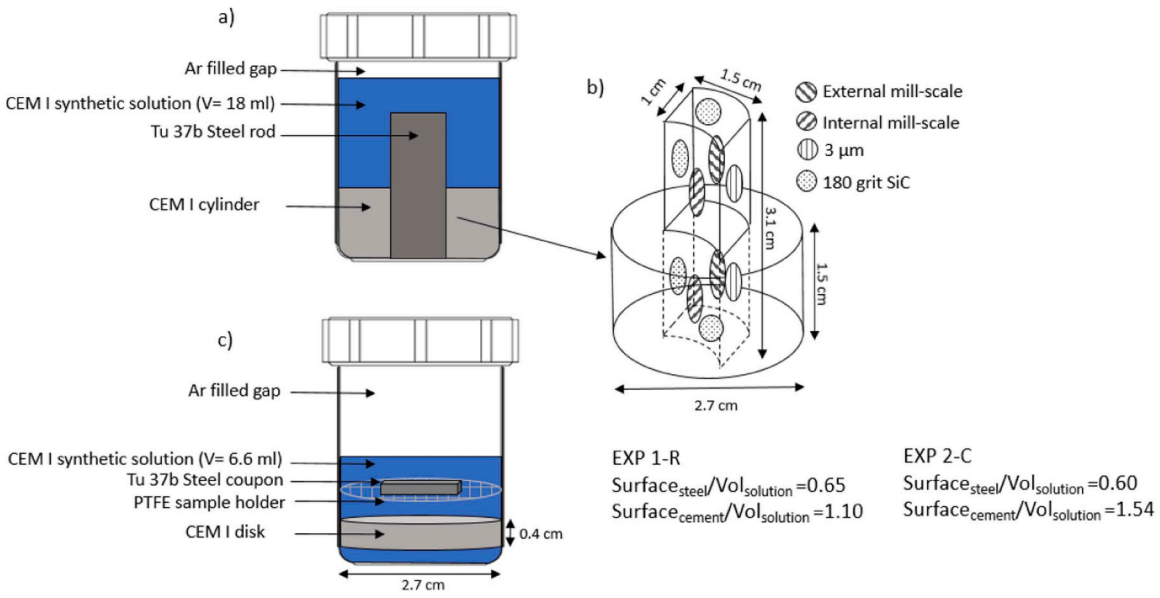

Fig. 2. (a) Set-up of the experiment 1-R (EXP 1-R) with (b) a schematic 3D-view of the grout-steel assembly put in the PTFE reactor; (c) set-up of the experiment 2-C (EXP 2-C).

was measured and quantified independently from the other elements and not recalculated stoichiometrically. The following standards were used for calibration: alumina (Al_2O_3) for O, halite (NaCl) for Na, sylvite (KCl) for Cl and K, periclase (MgO) for Mg, wollastonite ($CaSiO_3$) for Ca and Si, pyrite (FeS_2) for Fe and S. Non-quantitative EDX maps were collected at higher current intensities (1 nA) to optimize the quality of the mapping *vs* the acquisition time ratio.

2.5.2. X-ray diffraction (XRD)

To evaluate mineralogical evolution of HCP with time, XRD analyses were conducted directly on CEM I disk surfaces from EXP 2-C in a Bragg-Brentano geometry. The surface of some corroded steel coupons from EXP 2-C was also scanned in Bragg Brentano geometry. For both type of samples, a D5000 Bruker AXS diffractometer equipped with a Cu anti-cathode ($\lambda = 1.5406$ Å) operating at 40 kV and 25 mA was used. XRD scans were collected using an anti-air scatter screen in the range $2\theta = 5^\circ$ to 70° with a step size of 0.01° and 3 sec/step. These scans were first treated with the DIFFRACPLUS EVA software (Bruker) and the crystallographic open database (COD) was then used to attribute diffractions peaks to the corresponding mineralogical phases.

2.6. Corrosion rate determination by weight loss measurements

To assess the evolution of the corrosion rates with time, weight loss measurements were performed on steel coupons periodically retrieved from EXP 2-C, following the ASTM recommendation [34]. Briefly, steel coupons were taken-off from the reactors in an anoxic glove-box and immersed in 99 % pure de-aerated (under vacuum) ethanol for few seconds to stop corrosion. Then the coupons were dried, transferred outside the glove box, and immersed in the following successive baths: 15 % HCL – 5 % Hexamine solution, 5 % Na_2CO_3 and Isopropanol (99 %) with intermediate rinsing in deionized water between each bath. After this process, the coupons were weighted with an accuracy of 0.1 mg. This operation was repeated until the weight stabilization of the coupons. The corrosion rates were calculated from the following equation:

$$Corrosion\ rate\left(\mu m.y^{-1}\right) = \frac{3650 \times weightloss(mg)}{Density\left(\frac{g}{cm^3}\right) \times Area(cm^2) \times Time(days)} \quad (1)$$

with a density of 7.85 (g/cm^3) for steel.

2.7. Geochemical modelling

2.7.1. Modelling approach and code

The modelling of corrosion tests was performed with the reactive transport code HYTEC [35]. Under the present water-saturated conditions, the coupling between chemistry and diffusive transport was modelled by the following equation [42]:

$$\frac{\partial \omega C_i}{\partial t} = \nabla \bullet (D_e \nabla C_i) - \frac{\partial \omega \overline{C_i}}{\partial t} \quad (2)$$

where D_e represents the effective diffusion coefficient for all the dissolved species ($D_e = \omega D_p$ where D_p is the pore diffusion coefficient), ω is the material total porosity, and C_i and $\overline{C_i}$ are the species *i* mobile total concentration in solution and immobile total concentration in solid phases, respectively. The term $-\frac{\partial \omega \overline{C_i}}{\partial t}$ is the source/sink term that is driven by chemical reactions, whereas the other terms represent transport processes. HYTEC searches for an accurate solution to the multi-component transport problem using an iterative, sequential, so-called strong coupling scheme. The transport module of HYTEC is based on the representative elementary volume (REV) approach with finite volume calculation.

All chemical reactions were modelled at local thermodynamic equilibrium with truncated Davies activity correction model relevant for ionic strengths up to 0.5 molal. The aqueous chemistry included acid/base reactions, oxidation and reduction (redox) processes and aqueous complexation by inorganic ligands. The solid phase reactions dealt with dissolution and precipitation processes.

2.7.2. Thermodynamic database and solid phases

The 2019 version of Thermoddem (TDM) thermodynamic database was used [36]. TDM is a database for the thermodynamic properties of interest for hazardous and radioactive wastes, as well as the geochemistry of natural environments. TDM has also the advantage to allow calculations relevant for the present study relatively high temperature (80°C) conditions. In the model, the formation constant of (Fe)Si-hydrogarnet ($Ca_3Fe_2(SiO_4)_{0.84}(OH)_{8.64}$), and the formation constant of (Fe, Al)Si-hydrogarnet ($Ca_3AlFe(SiO_4)_{0.84}(OH)_{8.64}$) were derived from the study of Dilnesa et al. [37] and added to the TDM database. Table 3 gives the thermodynamic equilibrium constants of the iron phases considered in the modelling.

Table 3
Thermodynamic equilibrium constants of the iron phases considered in the modelling.

Solid phase	Formation reaction	25°C	Log K_f 60°C	100°C
Thermoddem database[(a)]				
Fe(element)	$Fe^{2+} + H_2O \rightarrow Fe + 0.5\ O_2(aq) + 2\ H^+$	−58.85	−52.03	−45.74
Goethite	$Fe^{3+} + 2\ H_2O \rightarrow FeOOH + 3\ H^+$	−0.36	0.75	1.77
Magnetite	$2Fe^{3+} + Fe^{2+} + 4\ H_2O \rightarrow Fe_3O_4 + 8\ H^+$	−10.36	−6.39	−2.75
Greenalite[(b)]	$3Fe^{2+} + 2\ H_4SiO_4 + H_2O \rightarrow Fe_3Si_2O_5(OH)_4 + 6\ H^+$	−21.77	−18.57	−15.64
Additional hydrogarnet				
(Fe)Si-HG	$3\ Ca^{2+} + 2Fe^{3+} + 0.84\ H_4SiO_4 + 8.64\ H_2O \rightarrow Ca_3Fe_2(SiO_4)_{0.84}(OH)_{8.64} + 12\ H^+$	−63.2	−52.2	−42.2
(Fe,Al)Si-HG	$3\ Ca^{2+} + Fe^{3+} + Al^{3+} + 0.84\ H_4SiO_4 + 8.64\ H_2O \rightarrow Ca_3AlFe(SiO_4)_{0.84}(OH)_{8.64} + 12\ H^+$	−66.8	−56.3	−46.8

(a) Blanc et al. (2012), version 1.10 (2019); (b) only used for the general Pourbaix diagrams (Fig. 16).

The minerals considered in the reactive transport modelling for dissolution and/or precipitation processes are the following: the discrete set of C-S-H with C/S from 0.8 to 1.6, portlandite ($CaOH_2$), ettringite ($Ca_6Al_2(SO_4)_3(OH)_{12}$:26 H_2O, monosulfoaluminate (Ca_4Al_2-SO_{10}:12 H_2O), monocarboaluminate ($Ca_4Al_2CO_9$:10.68 H_2O), hydrotalcite ($Mg_4Al_2O_7$:10 H_2O), Si-katoite $Ca_3Al_2(SiO_4)_1(OH)$ also denoted (Al)Si-HG, calcite ($CaCO_3$), gypsum ($CaSO_4$:2 H_2O), anhydrite ($CaSO_4$), arcanite $K_2(SO_4)$, Fe(element), goethite (FeOOH), magnetite (Fe_3O_4), (Fe)Si-HG ($Ca_3Fe_2(SiO_4)_{0.84}(OH)_{8.64}$) and (Fe,Al)Si-HG ($Ca_3AlFe(SiO_4)_{0.84}(OH)_{8.64}$).

2.7.3. Modelling grid and diffusive transport parameters

As shown in Fig. 3, the simulation grid considered a 2D in cylindrical (axis symmetric) coordinates based on the real dimensions and volumes of the reactor compartments of the EXP 1-R. In addition to 2D profiles, time evolution profiles were plotted in the reactor reservoir (P1), at the steel/solution interface (P2) and at the steel/cement interface (P3).

Table 4 gives the values of the effective diffusion coefficients that have been used to model the diffusive transport of soluble element occurring through the different components of the reactor at 80°C. The D_e coefficient associated to a similar Val d'Azergues CEM I hydrated paste was measured as 6×10^{-12} m^2/s at 20 °C [29]. The mean D_e coefficient of dissolved species in aqueous solution is around 1×10^{-9} m^2/s at 20 °C and 3×10^{-9} m^2/s at 80 °C. The D_e value inside the hydrated cement paste was estimated to be increased by a factor 5 while the temperature rose to 80°C, based on a previous study performed on a similar cement at 70°C [29]. For the sake of simplicity, the porosity evolution with time and temperature was not considered. The porosities of the CEM I hydrated paste and the solution were thus set to 0.35 and 1, respectively. Table 4 also provides for the D_e coefficients considered for the external raw of grid nodes corresponding to the surface of the steel rod in contact with the reactor solution and the CEM I paste. All the other inner grid nodes of the steel rod were never reactive in the modelling. The diffusive transfer at the steel/solution interface was fixed to the D_e value in the reactor reservoir (3×10^{-9} m^2/s) in all calculations. A sensitivity analysis was performed for steel/cement interface. The base case considered the same high D_e value as assumed for the steel/-solution, which corresponded to an open gap between the cement paste and the steel carbon steel rod. The D_e coefficient was then decreased to be identical to those of the hydrated CEM I paste, which stood for an almost perfect contact between the steel rod surface and the hydrated cement. Eventually, the D_e value at the steel/cement was even further decreased to determine the De value under which one only forms magnetite (discussed in Section 3.2.5). This simplified REV approach of the diffusive mass transfer was found to be useful to make distinctions between the different impacts that closed and open conditions may generate on corrosion mechanisms as discussed in Section 4.1.3. In this study, the closed conditions would correspond to a perfect contact between steel and cement, with only cement porewater solution at contact

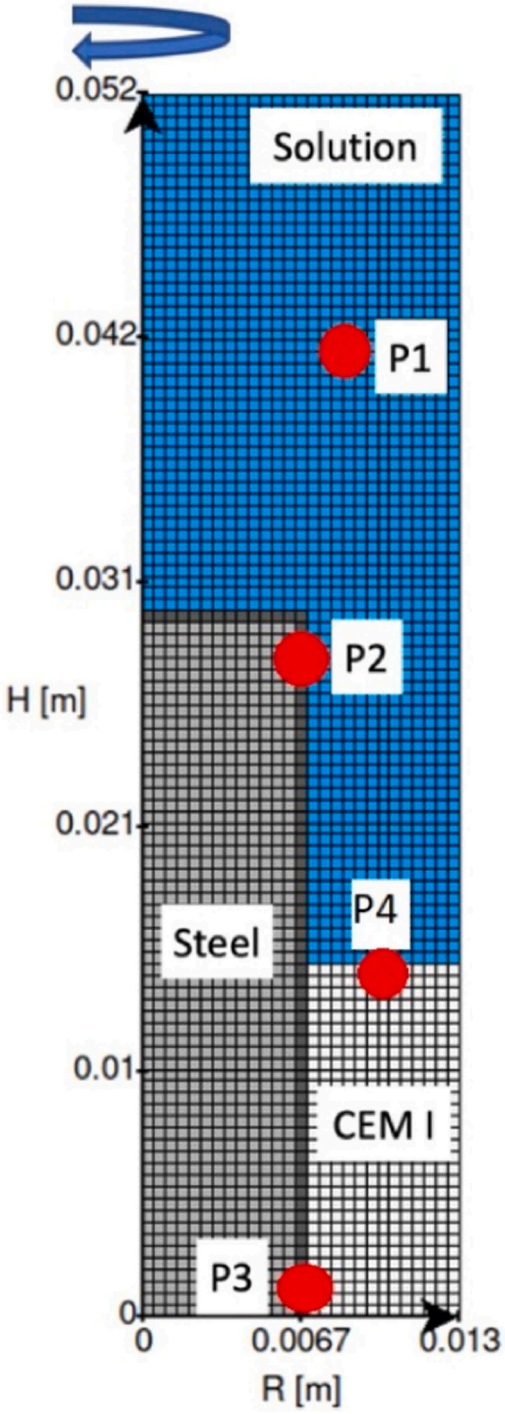

Fig. 3. Modelling grid in 2D-cylindrical geometry of the reactor in EXP 1-R; time evolution profiles were plotted in the reactor reservoir (P1), the steel/solution interface (P2), the steel/cement interface (P3) and the cement/solution interface (P4).

Table 4
Effective diffusion coefficients considered in the reactive transport modelling.

Material	Effective diffusion coefficient D_e at 80°C
Reactor reservoir	3×10^{-9} m^2/s
Hydrated cement paste HCP	3×10^{-11}
Steel/solution interface	3×10^{-9}
Steel/cement interface	
Base case	3×10^{-10}
HCP D_e	3×10^{-11}
Minimal low D_e	3×10^{-13}

with the cement steel interface whereas open state conditions correspond to an imperfect contact between steel and cement (e.g., fractures or imperfect encasing of the steel liner materialised by a gap filled with CEM I reservoir solution).

3. Results

3.1. Evolution of HCP mineralogy and solution chemistry

3.1.1. Initial modelled mineralogy and evolution with time and temperature

The modelling of the hydrated cement paste (HCP) initial mineralogy at 20 and 80°C was made at thermodynamic equilibrium based on the bulk composition of Table 1. Full hydration of all the initial cement phases was assumed. At 20°C, the calculated mineralogy of Table 5 is in good agreement with the data presented in Section 2.1.2. The main difference is that a small fraction of unreacted cement phases is still present in the real sample. Furthermore, hemicarboaluminate is absent in the model and the measured portlandite content is slightly lower than the calculated one, due to incomplete reaction of anhydrous cement phases in the samples.

The modelled evolution of the mineralogy was calculated for the specific geometry of EXP 1-R, whereas experimental information on the evolution of the mineralogy were obtained principally from EXP 2-C. However, only qualitative mineralogical evolutions are presented in this study and only used to confirm the principal trends of the modelled mineralogical evolution.

When the modelled temperatures increase up to 80°C, all monocarboaluminate and a fraction of ettringite dissolves to form calcite and (Al)Si-HG. Such transformation of monocarboaluminate to calcite is in agreement with the modelling results from the literature [38] but there is usually also a conversion of ettringite to monosulfoaluminate after 60°C [38]. The fact that (Al)Si-HG stabilizes ettringite in the specific case of the Val d'Azergues cement has already been discussed by Lalan et al. (2016) [28]. The same study has also demonstrated that ettringite fully dissolves in the model if one considers the pure Al-HG ($Ca_3Al_2[(OH)_4]_3$) named katoite instead of (Al)Si-HG in the calculated mineral assemblage [28]. The stability of these phases is related to the Al/ SO_4^{2-} in the modelled system and their stability constants. The formation of monosulfoaluminate is favoured when less Al is taken up by the hydrogarnet phases and hindered by the removal of SO_4^{2-}. XRD spectra of Fig. SI-1 indicates that most of the monocarboaluminate and all the ettringite present at the surface of the disks of EXP 2-C fully dissolved after 28 days at 80°C. The reactive transport model shows a progressive and complete dissolution of ettringite within one month (Fig. 4-a, b), leading to a concomitant increase of both (Al)Si-HG (Fig. 4-c) and portlandite (Fig. 4-d) content. The dissolution pattern progresses from the most external zones in direct contact with the reactor reservoir towards the core of the hydrated cement paste. There is no formation of monosulfoaluminate, partly due to the formation of (Al)Si-HG, and partly due to the dilution of the SO_4^{2-} concentration caused by diffusion into the reactor reservoir. The neoformation of portlandite is due to the release of Ca^{2+} induced by ettringite destabilisation, but also due to the high pH (thus high OH- ions content) condition imposed by the CEM I reservoir solution. Indeed, precipitation of portlandite was also observed at the surface of the cement paste in EXP 2-C and in the gap between cement paste and steel in EXP 1-R (Section 3.2.3).

The model did not capture other observed mineralogical evolution. The formation of arcanite at the surface of the cement disks was observed in EXP 2-C after 300 days of immersion (Fig. SI-1). EDX mapping performed on EXP 1-R cement cylinder after 350 days of interaction allow to clearly identify the dissolution of cement hydrates as well as the K enrichment occurring at the cement/CEM I reservoir solution interface (Fig. SI-2). Arcanite never precipitated in the model of the reactor at 80°C. The employed truncated Davies activity model may be inappropriate for more soluble minerals like arcanite but suitable for predicting the less soluble cement hydrate phases. Moreover, the very local dissolution was not significant in the model beside the full dissolution of the SO_4-cement phase (it would have required a strong refinement of the grid by setting a much smaller node size).

Table 5
Modelling of the initial mineralogy of the hydrated CEM I paste at 20°C and after a temperature increase to 80°C.

Mineral [mol/L of cement paste]	20°C	80°C
Portlandite	6.43	6.66
C-S-H 1.6	2.34 / 4.68[(a)]	2.21 / 4.42[(a)]
Ettringite	0.13	0.07[(b)]
Monocarboaluminate	0.12	-
(Al)Si-HG	0.12	0.27
Calcite	0.25	0.37
Hydrotalcite	0.05	0.05

(a) Normalized to 1 Si (Thermoddem considers 2 Si in the CSH formulae); (b) Ettringite dissolves in the HCP within 1 month (see Section 3.1.1).

3.1.2. Evolution of solution chemistry with temperature and time

Table 6 gives the calculated initial chemistry of the hydrated cement paste porewater at 20 and 80°C. Sorption of K^+, Na^+ and SO_4^{2-} on C-S-H was not considered in this modelling. At 20°C, the chemistry is typical of a young CEM I porewater with a very high pH (>13.5) that is mainly counterbalanced by Na^+ and K^+ at a total concentration around 10^{-1} mol/L. By comparison, the total concentrations of Ca^{2+}, H_4SiO_4 and Al^{3+} are relatively low, around 10^{-4} mol/L. The increase of temperature to 80 °C induces a decrease of the pH to 11.6 mainly due to the increase of the water dissociation product K_w with temperature. There is a significant increase of the SO_4^{2-} concentration around 10^{-1} mol/L by two orders of magnitude, whereas the total concentrations of Ca^{2+} and Al^{3+} slightly increase by about a factor 3. The total concentration of Si remains constant.

Fig. 5 shows the evolution with time of the chemistry of the synthetic water that was measured during EXP 1-R and modelled at 80°C. It is worth noting that the EXP 1-R PTFE reactor is "an open system" in the sense that the concentrations measured in the reservoir solution results from the diffusion, and thus dilution, of the porewater inside the reservoir solution and is not necessarily equal to the chemistry of the porewater contained in the porosity of CEM I material. As a matter of fact, the K^+ and Na^+ concentrations as well as pH in the reservoir solution were initially fixed to a high value that globally maintained the system under high alkaline chemical conditions.

Overall, there is a good to fair agreement of the model with the solution chemistry. The pH does not vary significantly over time (Fig. 5-a) in the model, whereas it slightly raised after 200 days in the experiment. It should be noted that the uncertainty of the measured pH data at such high pH and high temperature can be higher. Therefore, the modelled value is probably more indicative and is globally 0.3 unit lower than the measured one. The initial concentration in K^+, Na^+ and Cl^- were fitted on the experimental releases. They are close to the values found by Lalan et al. [28]. The modelled progressive increase of SO_4^{2-} and Ca^{2+} concentration reasonably simulates the experimental data (Fig. 5-b,c). Such evolution is due to the progressive ettringite dissolution and diffusion of these elements towards the reactor reservoir. Sulphate concentration is,

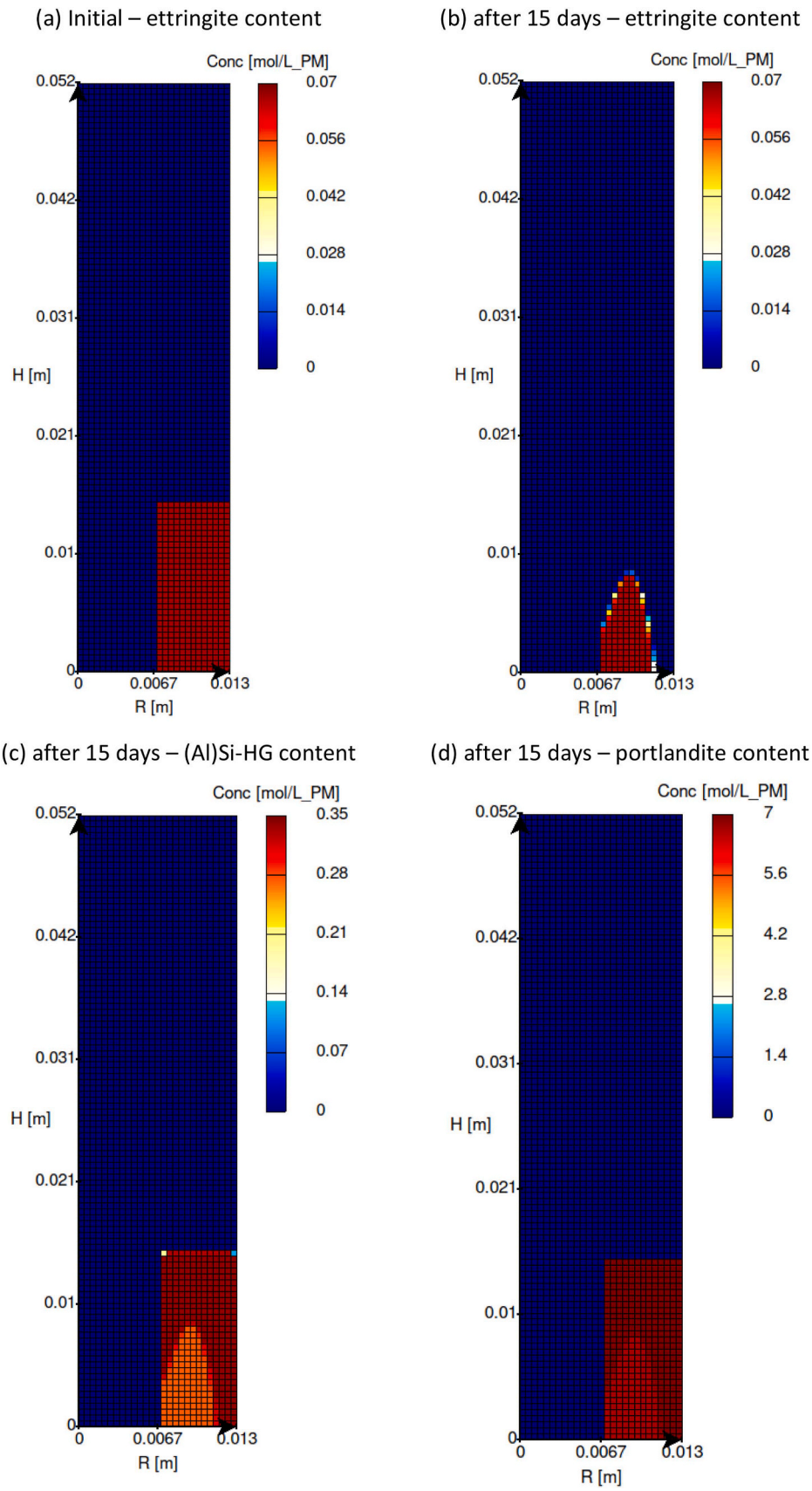

Fig. 4. Modelling of the dissolution of ettringite leading to a secondary precipitation of (Al)Si-HG and portlandite at 80°C.

Table 6
Modelling of the initial porewater chemistry of the hydrated CEM I paste at 20°C and after a temperature increase to 80°C.

Total concentration [mol/L]	20°C	80°C
pH	13.6	11.6
Ionic strength	0.43	0.43
K^+	3.5×10^{-1}	3.5×10^{-1}
Na^+	1.0×10^{-1}	1.0×10^{-1}
Ca^{2+}	8.0×10^{-4}	2.2×10^{-3}
Mg^{2+}	3×10^{-10}	5×10^{-9}
Al^{3+}	1.8×10^{-4}	4.2×10^{-4}
H_4SiO_4	6×10^{-5}	4×10^{-5}
HCO_3^-	1×10^{-5}	7×10^{-5}
Cl^-	5.0×10^{-2}	5.0×10^{-2}
SO_4^{2-}	1.2×10^{-3}	1.2×10^{-1}

nevertheless, moderately over-estimated by the model by factor a little bit less than 2. About half of the SO_4^{2-} anions can be sorbed onto the C-S-H phases in reality [39], process that was not included in the present modelling. The silica dissolved concentration is also well captured by the model although the modelling did not introduce any silica in the initial reservoir solution. The calculated CO_3^{2-} concentration is lower than the measured one by a factor 5 (Fig. 5-c). As the measured carbonate concentration tends to decrease with time, it may be due to a kinetic retardation of calcite precipitation whereas the model readily considers equilibrium with calcite. The model correctly predicts a low Al total concentration compared to the other elements, but the modelled concentration is higher than the experimental data by a factor 5 (Fig. 5-b). In the model Al is mostly controlled by the (Al)Si-HG solubility whereas Al may be also constrained by other phases in the real system (e.g., Al in C-(A)-S-H). It is worth mentioning that the formation of (Fe,Al)Si-HG in the modelling presented in Section 3.2.5 does not change the calculated Al concentration in the solution but that, inversely, the overestimation of Al concentration may have favoured the formation of (Fe,Al)Si-HG versus (Fe)Si-HG. Eventually, Mg concentrations are very low (outside the lower limits of the graphs), both in the experiment and the modelling.

3.2. Corrosion of steel

3.2.1. General aspect

Fig. 6 shows macroscopic features of the corrosion for some selected samples coming from both EXP 2-C and EXP 1-R. In EXP 2-C, all the retrieved coupons presented a uniform layer of adhering white crystals covering the whole surface of the coupons, as can be seen in Fig. 6-a, for a sample corroded for 93 days. In EXP 1-R, such whitish layer was also generally observed, but unequally distributed along the steel rod. Larger amounts of whitish crystal were observed in the vicinity of the cement plug, as can be seen in Fig. 6- b and indicated by the arrow, for a sample corroded for 28 days. Generally, dried samples coming from EXP 1-R also presented iridescent reflects as shown by the arrow, as can be seen in Fig. 6- c. As corrosion products are generally opaque, this observation indicates the precipitation of a very thin layer of corrosion products at the surface of the rods. Moreover, some fractured samples coming from EXP 1-R evidenced the presence of a white/translucent non adhering crystal layer at the surface of steel that was in contact with HCP as also shown by the arrow. These plate-like crystals were also observed at the bottom of the reactors. They were identified as portlandite later in the manuscript (Section 3.2.3)

3.2.2. Chemical and structural characterization of the corrosion products in function of time

Fig. 7 shows XRD patterns collected at the surface of two steel coupons coming from EXP 2-C. After 28 days of interaction, the XRD pattern revealed the formation of a phase belonging to the hydrogarnet group at the surface of the coupon. The peaks were correctly indexed using the

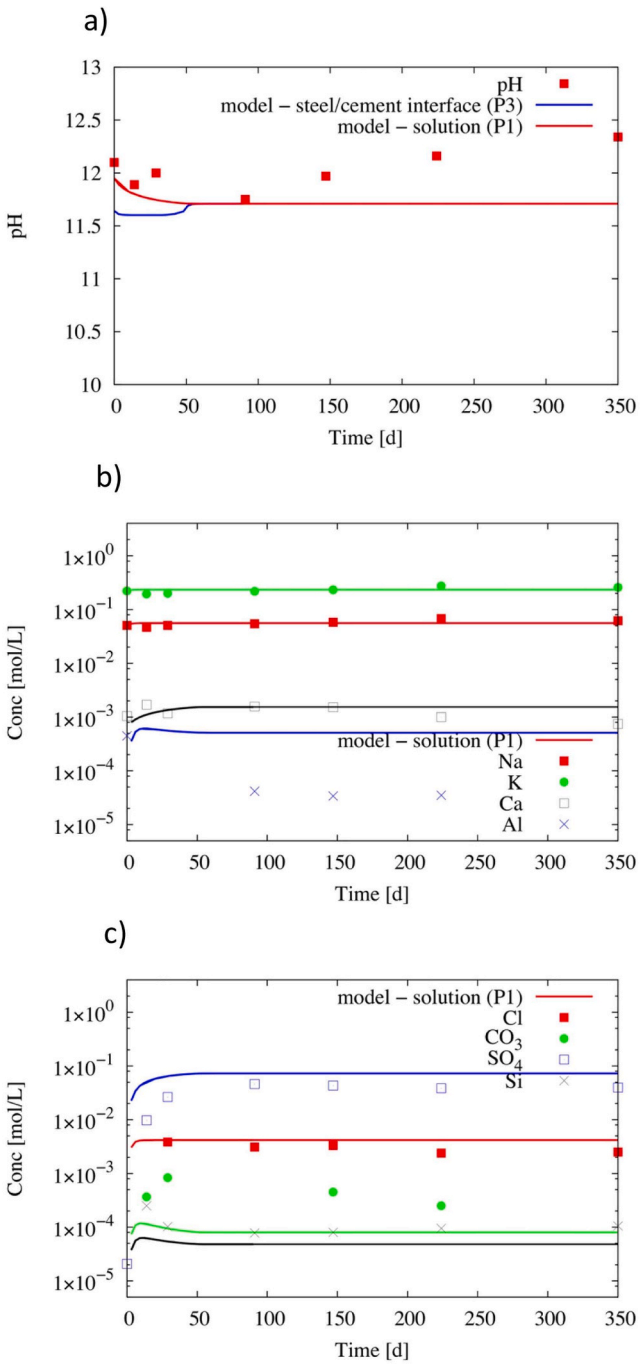

Fig. 5. Modelling of the change with time of the chemical composition in the reactor reservoir at 80°C; the experimental data are given as symbols. (a) Measured and modelled pH, (b) measured and modelled total aqueous concentrations in cations and (c) measured and modelled total aqueous concentrations in anions.

COD 1524032 corresponding to the $Ca_3Al_{1.096}Fe_{0.904}Si_{2.823}O_{12}H_{0.708}$ formula. After 300 days of interaction, the relative intensity of the peaks corresponding to (Fe,Al)Si-HG compared to (110) reflection of iron increased, signifying the growth of this phase with time. Reflections corresponding to portlandite were also identified at the surface of the coupon.

To gain information on the microstructure and composition of this phase, SEM-EDX analyses were conducted on a EXP 2-C coupon corroded for 28 days (Fig. 8). The SEM-SE (secondary electrons) pictures revealed the presence of rounded shaped crystals covering almost

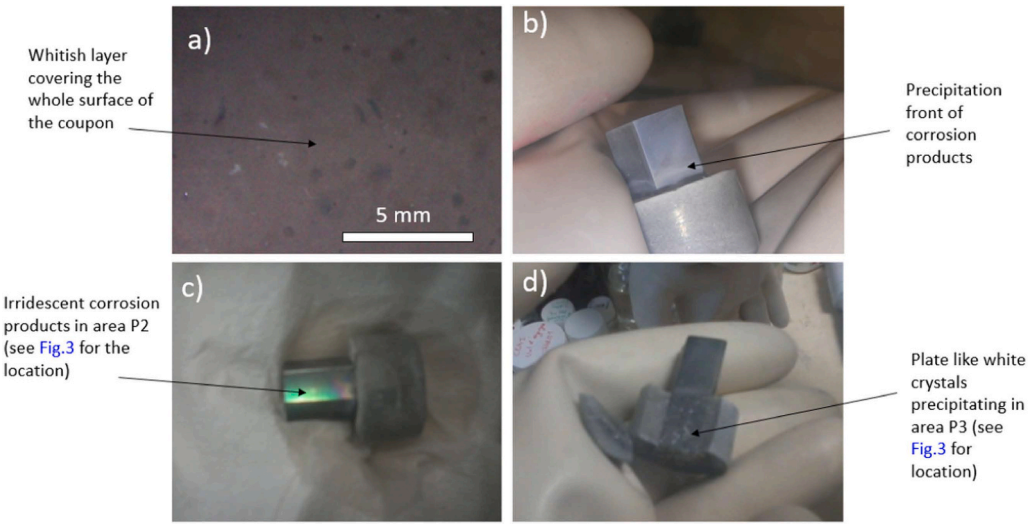

Fig. 6. Pictures of corroded samples coming from (a) EXP 2-C after 93 days of interaction and from (b) EXP 1-R after 28 days and (c) 254 days of interaction showing both steel/solution interface and (d) steel-cement interface.

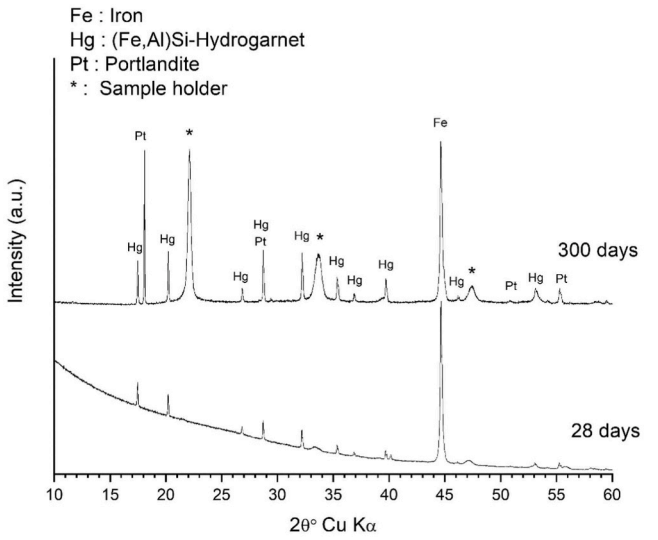

Fig. 7. XRD patterns of the surface of the metallic coupons coming from EXP 2-C after 28 and 300 days of interaction.

entirely the surface of the coupon. The composition of this phase is reported in Fig. 8-b and the corresponding formula, considering only major elements, would be $Ca_{3.2}Fe_{1.25}Al_{0.8}SiO_{4.6}(OH)_{7.43}$ normalizing the atomic proportion to 12 oxygens which correspond to garnet formulas. Such formula is very close to (Fe,Al)Si-HG formed in old mortars ([31]). Moreover, low amount of S (≈ 1 %) was detected in this phase, as already observed by Kyritsis & al, 2009 [40] and by Passaglia et Rinaldi, 1984 in the Al pure end member Si-katoite [41]. The presence of KCl grains was also depicted at the surface of the coupon in a relatively low amount.

3.2.3. *Effect of direct contact vs spatial heterogeneity*

In EXP 1-R, SEM-EDX observations also revealed the formation of Ca, Si, Fe, Al, O containing phase on the metallic surface in contact with both the reservoir solution (location P2 in Fig. 3) and the CEM I plug (location P3 in Fig. 3) from 14 to 350 days. As an example, SEM-EDX mappings of the two interfaces P2 and P3 at 350 days are presented in Fig. 9. Due to the low thickness and density of the CPs (corrosion products) layer formed during the experiment, meaningful EDX analyses of the cross sectioned samples were only obtained for the sample immersed for 350 days in the reservoir solution.

The Si/Ca *vs* (Al+Fe)/Ca ratios of the corrosion product layer observed at 350 days for EXP 1-R samples at the steel/solution interface (P2) and steel/cement interface (P3) are presented in Fig. 10-a and compared with the same ratio of the (Fe,Al)Si-HG phase observed at the surface of the coupon in EXP 2-C at 28 days. The relatively low discrepancies between the chemical compositions of the corrosion products observed in EXP 1-R and EXP 2-C suggest that (Fe,Al)Si-HG also formed in EXP 1-R at both interfaces P2 and P3. The Si/Ca *vs* Al/Fe ratios of the same samples are also shown in Fig. 10-b. These ratios vary significantly at the two different interfaces P2 and P3, with higher amount of Al at P3. This difference can be explained (i) by the progressive consumption of Al into (Fe,Al)Si-HG along the steel rod from the bottom to the top of the reservoir, but also (ii) by the difference in the Al concentration between P2 and P3 interface. Indeed, a small volume of reservoir solution filled the gap between the steel and the cement interface (interface P3) due to the HCP shrinkage after hydration. In this small volume, the Al concentration was probably much higher than the concentration of the reservoir solution. The fact that the HCP surface is not strongly leached at the interface with steel (interface P3) (Fig. 9) compared to the interface with reservoir solution (interface P4) (Fig. SI-2) indicates that exchange and renew of the solution was limited in this gap. The Al/Fe ratio of the (Fe,Al)Si-HG coming from EXP 2-C (28 days) is comparable to the one associated to the (Fe,Al)Si-HG phase observed at interface P3. This is to link with the difference in Al concentration of the reservoir solution in EXP 1-R (e.g., 3.7×10^{-5} mol/L at 224 and 350 days) and EXP 2-C (e.g., 2.04×10^{-4} mol/L at 300 days) for a given time of interaction).

Fig. 11 shows that, despite the fact that iron migration was very limited in HCP due to its rapid consumption to form (Fe,Al)Si-HG at the steel/cement interface, transformation of the surrounding HCP medium could be locally observed. From the steel to the cement, the transformed HCP medium is first enriched in Fe and O and then enriched in Ca, Si, Al, S, Fe and O. This result suggest that an initial layer of Fe hydr(oxide) transformed into (Fe,Al)Si-HG. Such transformation involved diffusing elements from the HCP porewater solution. It should be noted that the presence of iron (hydr)oxides was observed in very rare occasions and sporadically at the interface P3. Such iron (hydr)oxides were probably formed in the early stage of the experiment and even during the sample preparation.

Finally, a great amount of large plate-like crystals of portlandite precipitated in this gap, as confirmed by Ca and O mappings (Fig. 9) and as observed macroscopically (Fig. 6-d).

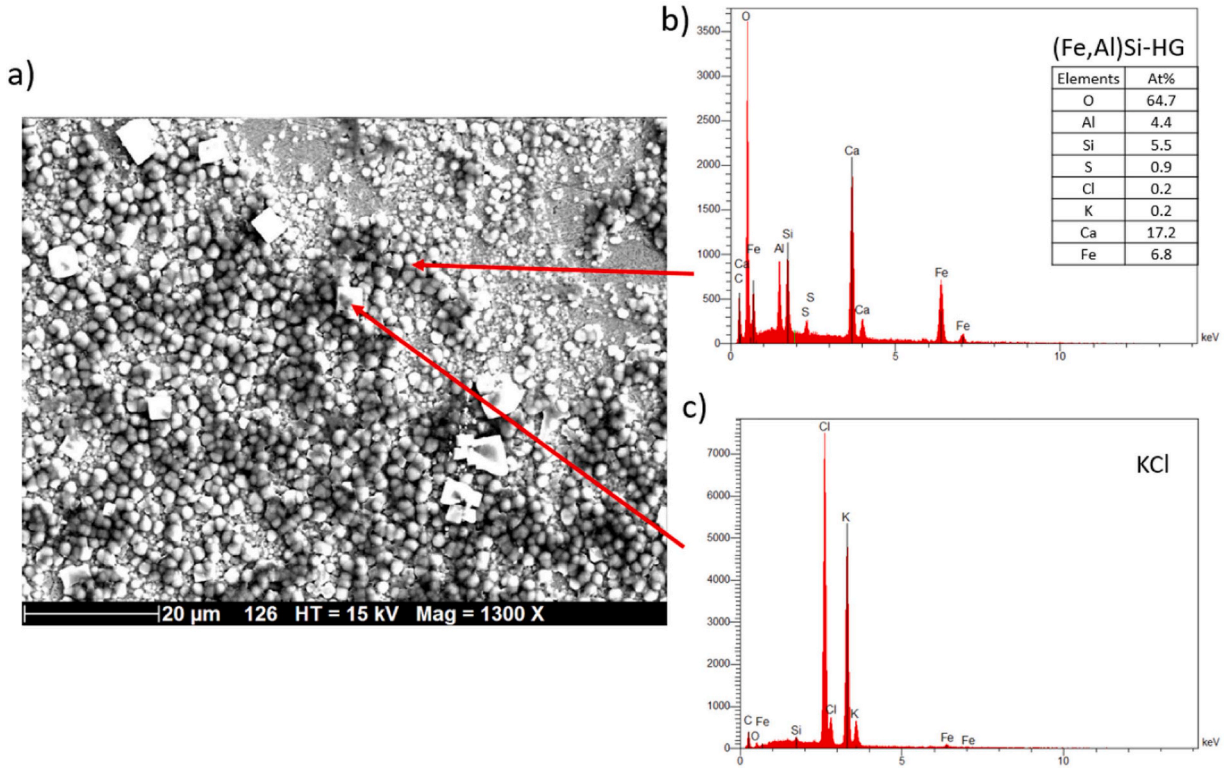

Fig. 8. (a) SEM-BSE picture of the surface of the coupon immersed for 28 days in the CEM I reservoir solution (EXP 2-C) along with (b) EDX spectra of the principal corrosion products and (c) precipitates observed. The given chemical composition of (Fe,Al)Si-HG corresponds to the mean of seven analyses.

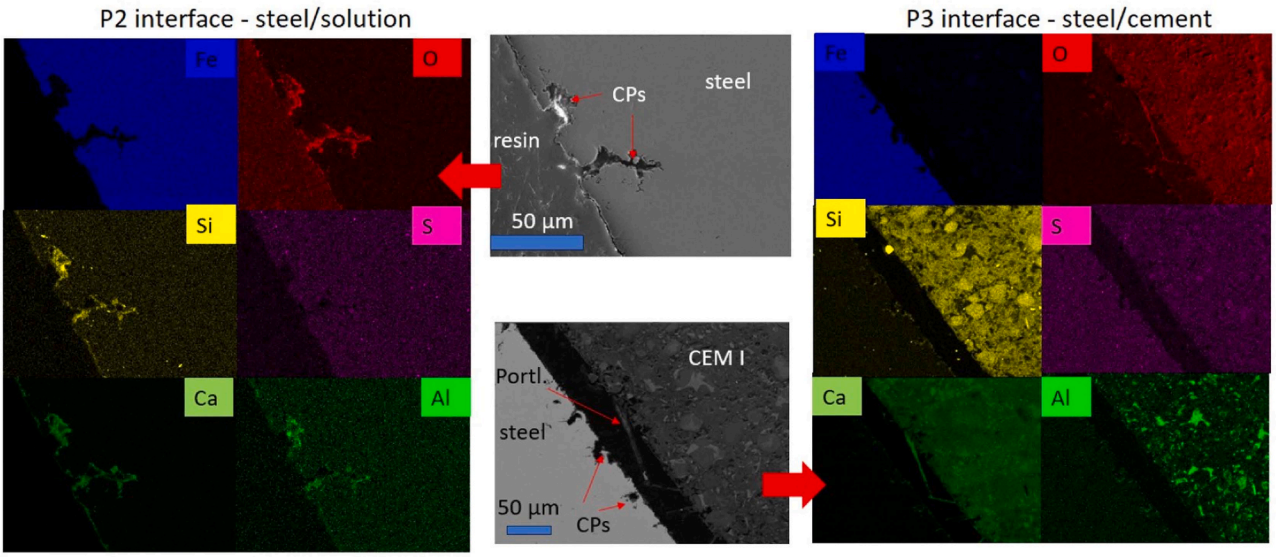

Fig. 9. SEM-EDX mapping of the interface between carbon steel mill scale layer and the two different interfaces P2 (steel/solution) and P3 (steel/cement) (EXP 1-R) after 350 days of interaction. *Cps =corrosion products, Port.= portlandite.*

3.2.4. Corrosion rates

3.2.4.1. Generalized corrosion rates from EXP 2-C. Fig. 12 shows the evolution of the corrosion rate with time, obtained by weight loss measurement for EXP 2-C carbon steel samples. As expected, the corrosion rate dropped with time and the decrease can be approximately described with an exponential decay law, as generally observed in experiments conducted in similar conditions (e.g., [14]). However, the predicted long term corrosion rates are quite high (approximately 0.3 µm/y) and 2 orders of magnitude higher than those observed in the latter 6 years long experiments where corrosion rate were derived from hydrogen pressure measurements (e.g.; [14]). It should be noted that mass loss measurements provide results with relatively high discrepancies (≈10 % relative error on three different coupons for the present experiment) and that more adapted technics to measure very low corrosion rate (e.g., [19]) would have been more suitable to determine more precisely the residual corrosion rates.

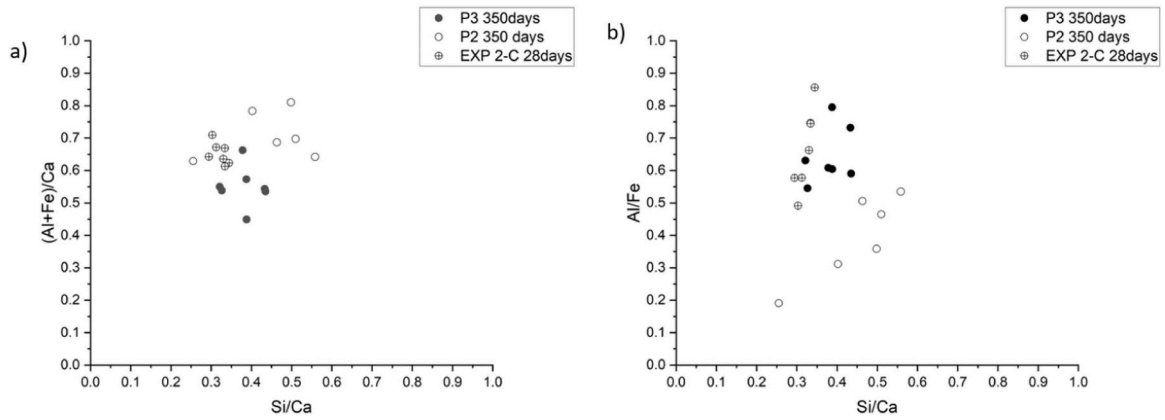

Fig. 10. Comparison of the (a) (Al+Fe)/Ca vs Si/Ca and (b) Al/Fe vs Si/Ca ratio evolution of the corrosion product with time at the direct contact with cement (P3) and at direct contact with the reservoir solution (P2) for EXP 1-R. Similar ratios were also measured on CPs coming from EXP 2-C, formed in direct contact with solution.

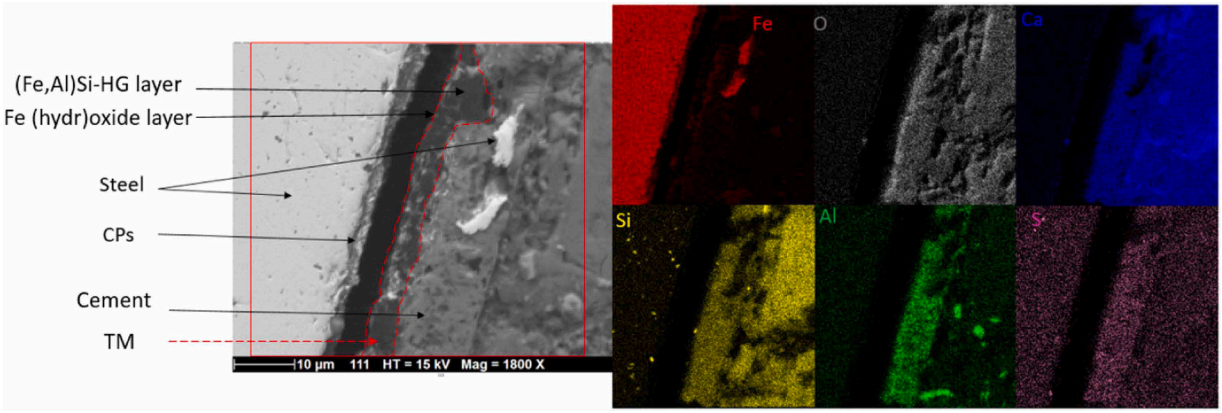

Fig. 11. SEM-EDX mapping of the interface between carbon steel (180 grit ground surface) and cement after 93 days of interaction. *CPs = corrosion products, TM = Transformed Medium.*

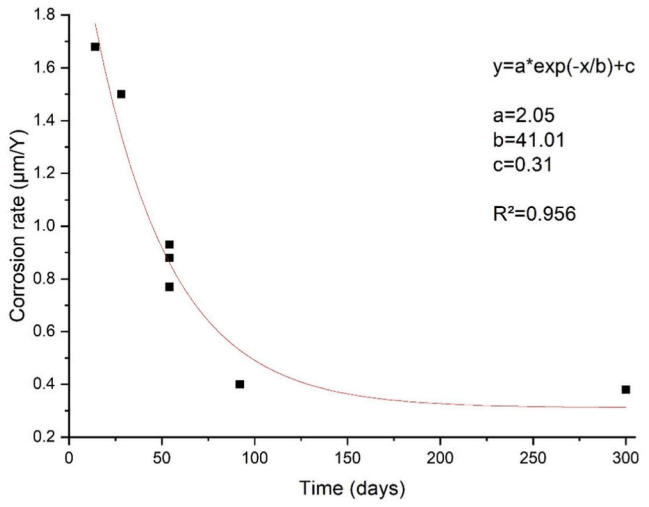

Fig. 12. Corrosion rates measured by weight loss measurements on EXP 2-C carbon steel samples and fitting of the data with an exponential decay law.

3.2.4.2. Effect of the mill-scale layer. In EXP 1-R, different types of initial steel surface conditions (i.e., presence of mill-scale layer, rough or polished surface) were exposed to the synthetic cementitious solution in order to assess the role of the metallic surface nature on the corrosion rates. In particular, the tube utilized for the BACUCE *in situ* and mock-up experiments presented a microstructurally heterogeneous mill-scale layer more representative of the surface of steel casing that would be involved in deep geological repository than the well-prepared coupon following ASTM method. It was not possible to measure corrosion damage on such surfaces, due to the relatively low corrosion rates obtained in this environment. However, as (Fe,Al)Si-HG was found to be the unique corrosion product that formed, it was possible to follow the formation of this phase with time through SEM mappings. For that purpose, calcium was used as a marker because of its relatively high content in (Fe,Al)Si-HG and its absence in the steel composition, in the mill-scale layer and in the polishing grains (SiC) that could be trapped in the porous area of these layers. However, as portlandite could have also precipitated at the surface of the steel layers, care was taken to select area without portlandite grains, and the nature of the CP (corrosion product) layer was controlled by the overlapping of Ca, Si and Al EDX maps. The maps were collected using similar acquisition time to further compare them to each other. Moreover, the thin section which was observed and analysed was located at approximately the same distance from the cement plug for all sampling time to limit the spatial impact of such measurement. Indeed, the distribution of the CPs is not uniform spatially, but a propagation front of CPs is rather observed from the cement plug to the upper part of the steel rod (see Fig. 6b). Fig. 13-a present the evolution of the Ca maps of mill scale layers exposed to the synthetic cementitious solution with time. A careful observation of these mappings revealed that the (Fe,Al)Si-HG layers rather densify with time than increase in thickness (i.e., the signal intensity increase but the

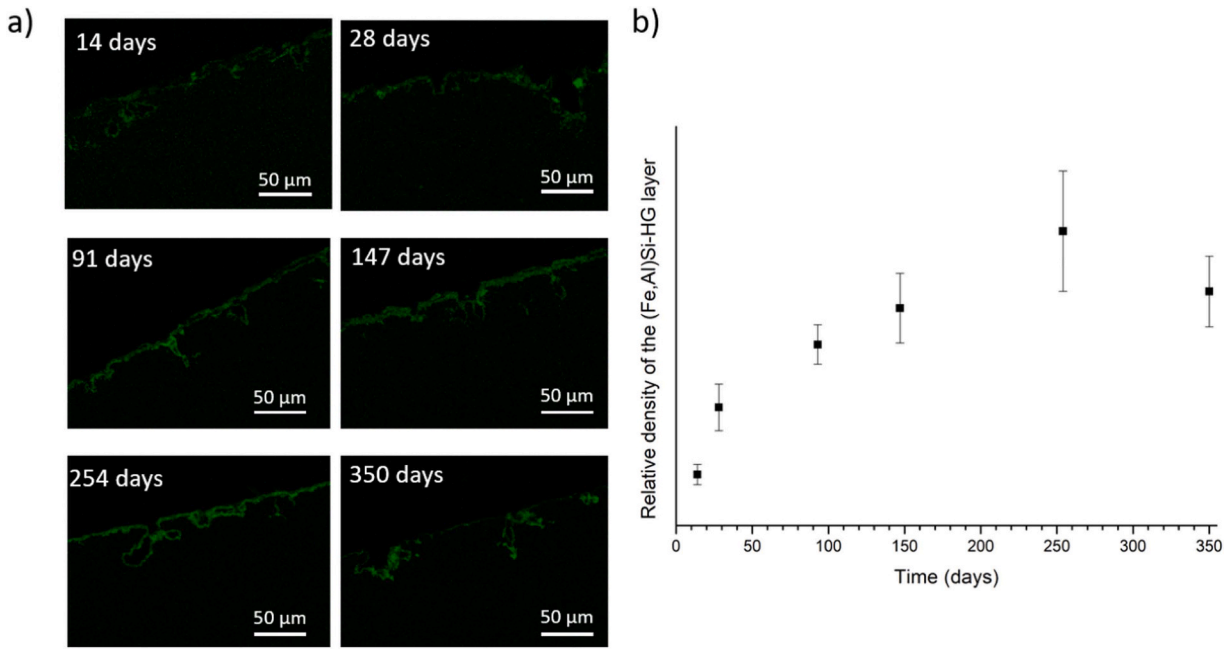

Fig. 13. (a) Ca SEM-EDX mapping of the interface between carbon steel mill scale layer and solution for EXP 1-R in function of time along with (b) the relative density of the (Fe,Al)Si-HG layer.

thickness of the marked zone is stable). In order to derive qualitative results from these observations, the relative density of these (Fe,Al)Si-HG layer was determined by grey level analyses using ImageJ ®. In practice, the percent of pixels corresponding to the (Fe,Al)Si-HG layer, normalized by the length were plotted *vs* time (Fig. 13-b). The dispersion on the results were obtained by the analyses of two different areas per sample and using two different magnifications (x200 and x500). This figure shows that the relative density rapidly increased with time until reaching a plateau, indicating that further formation of (Fe,Al)Si-HG was hindered by the precipitation of a dense diffusive barrier of (Fe,Al)Si-HG on the carbon steel surface able to clog the heterogeneities of the mill-scale surfaces.

3.2.5. *Modelling of the corrosion process*

The modelling of the initial mineralogy and solution chemistry when the temperature increases from 20 to 80 °C, and their evolution over one year in the "open" reactor system was developed in Section 3.1.2. The present section goes a step further by including steel corrosion in the model. Steel was modelled as a pure metallic Fe(0) phase, denoted Fe (element) in the TMD database under kinetic-control with a selected constant corrosion rate of 1 µm/y consistent with the experimental values measured within the first six months of interaction.

Fig. 14-a shows the 2D-profiles of the formation of the corrosion products after 6 months for the base case detailed in Table 4. The anoxic corrosion process liberates Fe ions in solution at both the steel/cement and steel/solution interfaces. It also liberates H_2 that leads to a steady-state value of the redox potential Eh around −580 mV (vs. SHE) at pH 12. In parallel the chemistry of the reactor reservoir is almost constant after 1 month, especially the stock of dissolved Al, Si and Ca brought by cement phase dissolution (Fig. 5). In the base case (highest D_e at the steel/cement interface), (Fe,Al)Si-HG is the only corrosion products depicted over the whole surface of the steel rod. (Fe)Si-HG as well as magnetite precipitation is never predicted, either at P2 or P3. However, the overestimation of Al concentration in the model (Fig. 5) could have favoured the formation of (Fe,Al)Si-HG versus (Fe)Si-HG. Note that in time, the incorporation of Al in another phase like C-(A)-S-H can lead to a decrease of the dissolved Al. The relatively high diffusion coefficient at the steel/cement interface (gap) increases the diffusive flux of Ca and Si from the reservoir solution, but also from the cement itself, feeding the formation of (Fe,Al)Si-HG. When the D_e value at the steel/interface is equal to the one associated to HCP, the lower diffusive transfer at the steel/interface (moderately) enhances the proportion of magnetite at P3, even if (Fe,Al)Si-HG is still the main corrosion product (Fig. 14-c and d). Again, (Fe)Si-HG is not predicted to precipitate. Such low D_e value implies that the elements forming (Fe,Al)Si-HG mainly diffuse from the HCP porewater directly close to the steel, and not from the reservoir solution. It is worth mentioning that in an intermediate case between high and low HCP D_e, magnetite that was first formed at P3 progressively redissolves (Fig. 14-c) to form an additional amount of (Fe,Al)Si-HG (Fig. 14-d). The case in which magnetite becomes the main corrosion product at the steel/cement interface requires to decrease the D_e value to 3×10^{-13} m^2/s at such interface (Table 4). This value is significantly lower than the D_e coefficient estimated in the present cement paste at 80°C (3×10^{-11} m^2/s), and still moderately below D_e coefficients (about 10^{-12} m^2/s) measured in concretes at ambient temperature [42]. On the contrary, 3×10^{-13} m^2/s is much higher than the D_e values assumed for diffusion though the magnetite corrosion layer (from 10^{-15} m^2/s to 10^{-19} m^2/s) [43]. Therefore, this sensitivity case can also be seen as representative of the beginning of the formation of a diffusive barrier made of magnetite that hinders diffusive transfer. Fig. 15 illustrates the difference of total Si concentrations along the steel/cement interface that decreases from more than 10^{-5} mol/L (highest D_e) to 10^{-6} mol/L (lowest D_e). In the latter case, the silica concentration is too low at the steel/cement interface as to promote (Fe,Al)Si-HG formation along this latter.

4. Discussion

4.1. *The combined effect of temperature, pH, Eh and chemistry on (Fe,Al)Si-HG precipitation*

4.1.1. *Effect of temperature*

Temperature impacts the kinetics of the corrosion processes, including the corrosion rate and the kinetics of electrochemical reactions. Those aspects were not developed in this study based on thermodynamic equilibrium models, although kinetics can have a significant effect on (Fe,Al)Si-HG formation. Nevertheless, temperature can be considered as a direct and indirect parameter influencing the formation

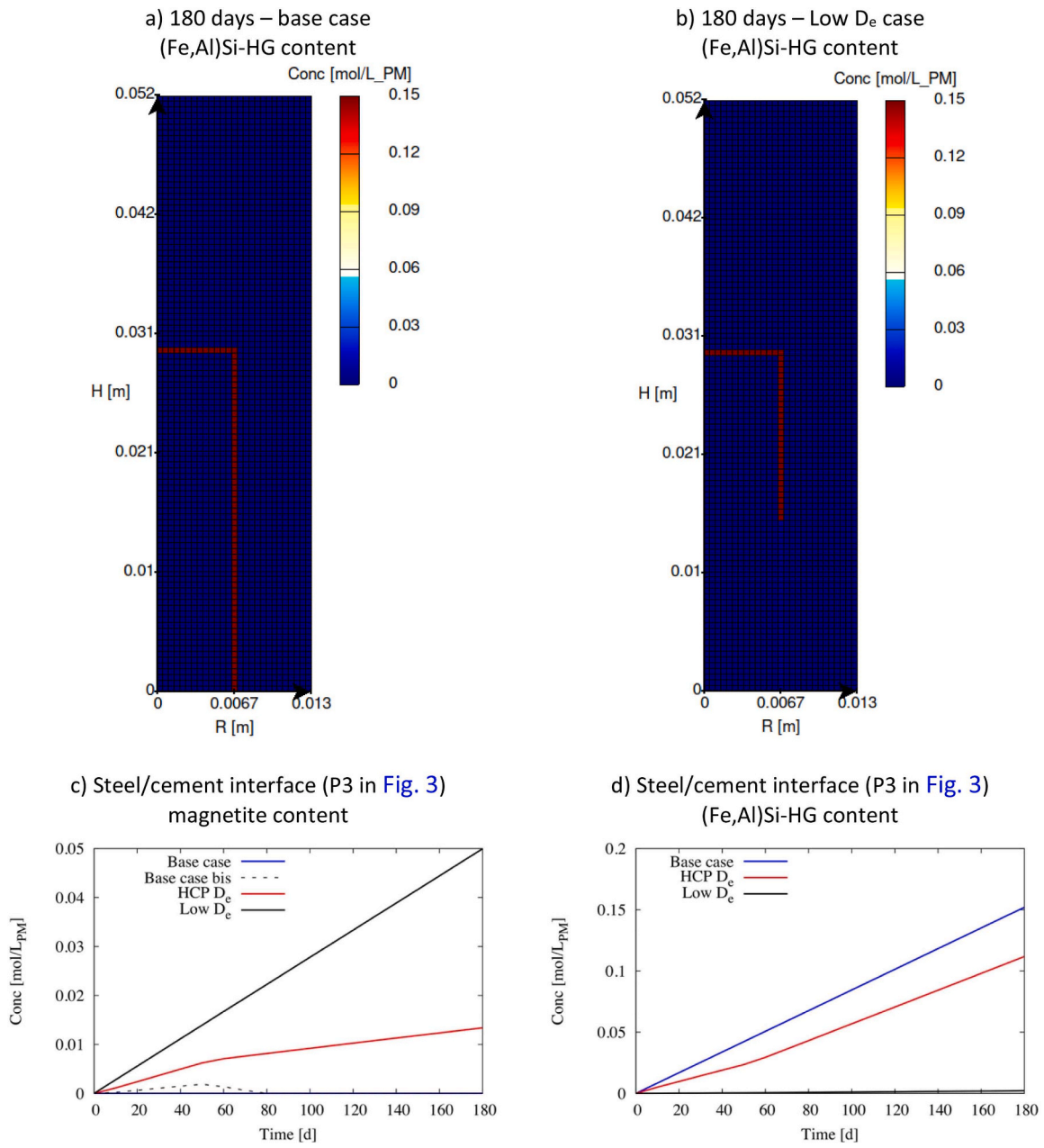

Fig. 14. Modelling of the formation of corrosion products after 180 days at 80°C due to steel anoxic corrosion at a constant rate of 1 μm/y according to a sensitivity analysis on the diffusion coefficient along the steel/cement interface (P3 in Fig. 3).

of (Fe,Al)Si-HG. The principal and direct impact of temperature is of kinetical order. Indeed, (Fe,Al)Si-HG is generally synthetized at a temperature between 80 and 450°C ([37,40,44]). In Portland cement, the formation of (Fe,Al)Si-HG is scarce ([30,45]), but it is enhanced with time ([31,46]) and/or at elevated temperature [38,47–50]). Anecdotally, it can also form rapidly in specific cements at lower temperature, as in Portland cement with an excess of C_4AF ([28]) or with an excess of Fe $(OH)_3$ ([51,52]).

In addition to the kinetics of precipitation, several other impacts induced by temperature that promote the formation of (Fe,Al)Si-HG can be considered. The first one is linked to the thermodynamics of the pH/Eh stability domain of CPs that is dependent of temperature. Fig. 16 shows the Pourbaix diagrams calculated at 25 and 80°C for the simplified Fe – O – Ca – Al – Si system. The thermodynamic stability domain of (Fe,Al)Si-HG expands at 80°C along both the pH and Eh axis, at the cost of the goethite and magnetite domains.

Higher temperature usually favours a higher degree of hydration of the cement clinker phases and promote the dissolution of cementitious hydrates, such as ettringite. This indirect effect of temperature that leads to ettringite dissolution induces the release of Ca, Si, and Al into the system and thus enhances the formation of (Fe,Al)Si-HG. The last indirect impact of temperature increase that can be considered is associated to the modification of the cementitious assemblage microstructure that can increase the diffusion of the dissolved elements from the cement toward the interface to interact with steel (e.g., [53]). Such diffusive properties are essential, especially for long term corrosion processes.

4.1.2. *Effect of pH*

Hydrous garnet phases are commonly stable in high pH alkali and alkaline earth rich systems at ambient and hydrothermal conditions ([37,40,41,54–56]). At later stages of cement evolution after leaching of the alkalis, the pH of the cement solution is set by the equilibrium of

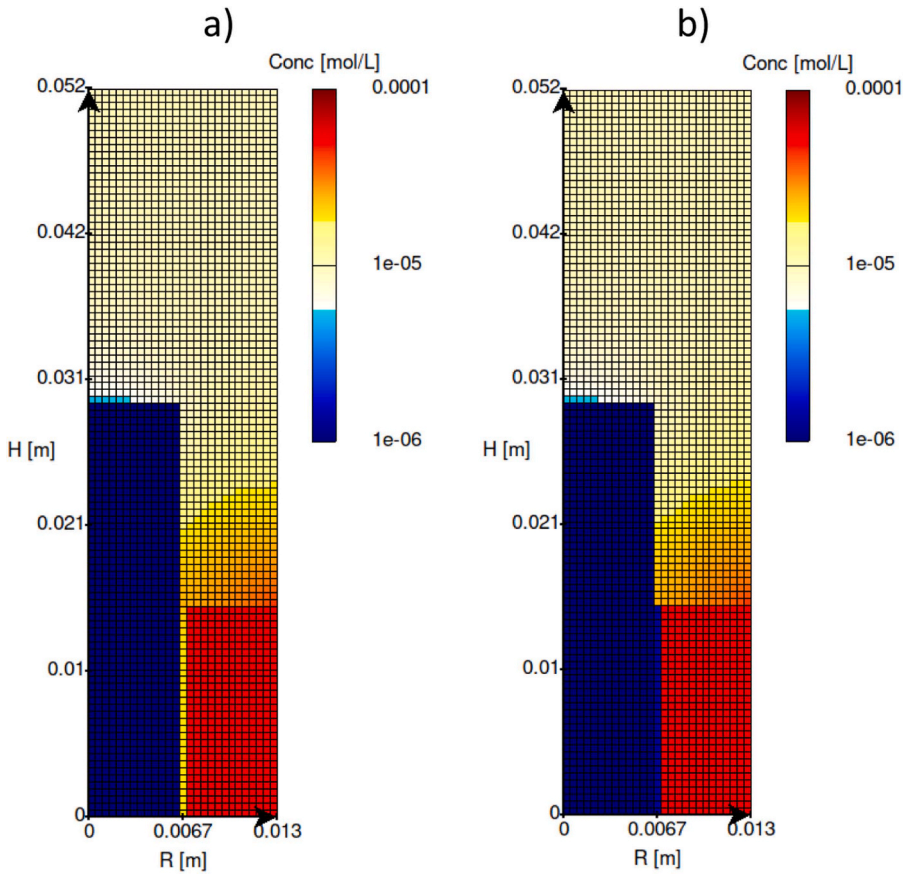

Fig. 15. Modelling of the dissolved silica total concentration according to the sensitivity analysis on the diffusion coefficient along the steel/cement interface at 180 days with (a) base case and (b) low De case.

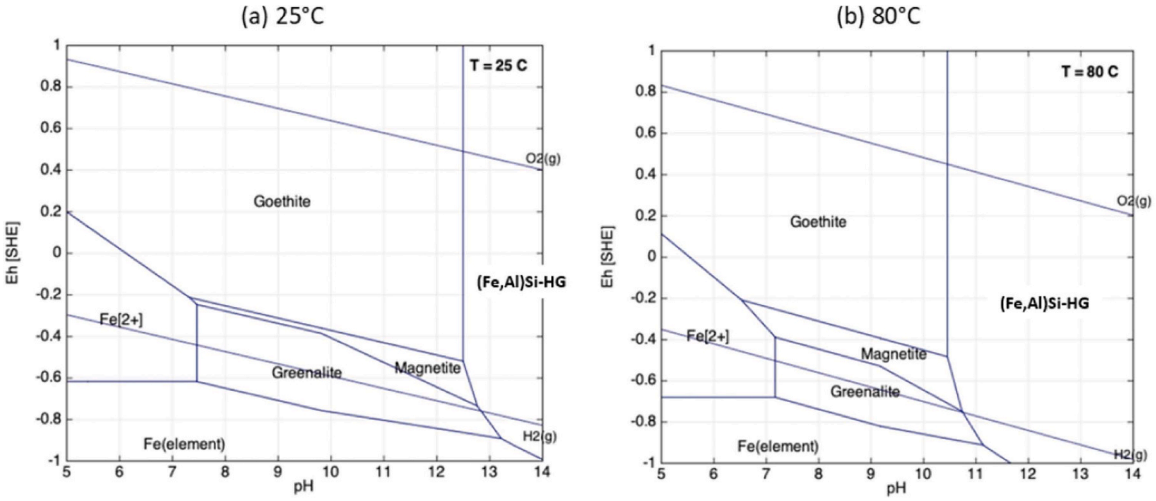

Fig. 16. Pourbaix diagrams of the Fe – O – Ca – Al – Si system calculated with CHESS at (a) 25°C and (b) 80°C; activity $Fe^{2+} = 10^{-6}$, activity $Ca^{2+} = 10^{-3}$, activity $Al(OH)_4^- = 5\times10^{-5}$, total $H_4SiO_4 = 10^{-4}$.

portlandite and C-S-H phases at high values. As shown in Fig. 16, iron (oxi)hydroxides and iron phyllo silicates are predicted to be stable instead of (Fe,Al)Si-HG at lower pH values. Such conditions would be found in low pH cements or at clay/steel interfaces. Experimental evidences of the formation of magnetite and iron (II) containing phyllosilicates are reported for both systems (e.g., [27,57], respectively).

4.1.3. Effect of composition and competition of (Fe,Al)Si-HG with other cementitious phases

Si-free katoite (C_3AH_6) is a major phase in aluminate cement [58] but Si-free C_3FH_6 is known to be thermodynamically unstable in Portland cement due to the presence of silica [37]. Indeed Si can stabilize the hydrogarnet structure for a wide range of cement compositions and temperatures from 5 and 85°C [59]. (Al, Fe)-monosulfate, (Al, Fe)-ettringite solid solutions, Fe-monocarbonate, and hemicarbonate

phases are stable in the absence of silica [37,60,61]. Thus, formation of hydrogarnet in Portland cement requires the presence of Ca, Al and/or Fe as well as Si in the solution. Section 3.2.5 and Fig. 15 indicated that (i) the dissolved silica concentration brought by cement phase dissolution can have a significant impact on the corrosion products of steel, and (ii) that (Fe,Al)Si-HG can form at relatively low silica concentrations (10^{-6} – 10^{-5} mol/L), controlled by the equilibrium with high Ca/Si C-S-H. On the contrary, Fig. 17 shows that the Ca^{2+} concentration has been relatively high to favour (Fe,Al)Si-HG against other corrosion products. Ca^{2+} concentration in the CEM I porewater is controlled by portlandite equilibrium and, therefore, should be low when the pH is high as for the present conditions. However, as the temperature increased to 80°C, it favoured the dissolution of ettringite that induced an increase in Ca^{2+} ions concentration (Table 6) that could be further used to form (Fe,Al)Si-HG.

Competition between C-(A)-S-H and (Fe,Al)Si-HG formation is also of importance in such system. Fig. SI-3 shows the speciation diagrams of the Fe – O – Ca – Si system including C-S-H and (Fe)Si-HG as a function of pH and of the activity of Si and Fe at 25 and 80°C. Those diagrams mostly indicate that temperature always enhances the formation of FeSi-HG instead of C-S-H phase. Similar results were obtained for the Ca-Si-Al-Fe-O system, where C-S-H were replaced by C-A-S-H/straetlingite and (Fe)Si-HG by (Fe,Al)Si-HG. With respect to the competition for dissolved Fe, C-S-H phases can sorb and/or incorporate Fe^{3+}, and to a lesser extent Fe^{2+}, independently of their Ca/Si ratio [62,63]. Siramont et al. [51] studied at ambient temperature the fate of iron in a Ca-Si--Fe-H_2O system for different pH and for iron concentrations between 1 and 4 mmol/L. Results showed that for pH>11, most of the dissolved Fe ions are used initially to form ferrihydrite phase, that would then be transformed into FeSi-HG, whereas only merely 3 % of the Fe content goes in the C-S-H phase.

4.1.4. Redox conditions

The redox conditions may also play a role on the nature of the corrosion products since (Fe,Al)Si-HG is a pure Fe^{3+} phase whereas magnetite is a mixed Fe^{2+}-Fe^{3+} phase. In the corrosion mechanism proposed by Pally et al. [26], prior to the formation of (Fe,Al)Si-HG, Fe^0 is oxidized to $Fe(OH)_2$ that further evolves to magnetite according to the Schikorr reaction:

$$Fe + 2\,H_2O \rightarrow Fe(OH)_2 + H_2\uparrow \quad (3a)$$

$$3\,Fe(OH)_2 \rightarrow Fe_3O_4 + H_2\uparrow + 2H_2O \quad (3b)$$

Both reactions produce H_2 that can impose strongly reducing conditions in the system. Fig. 17 shows that strongly reducing conditions may favour magnetite against (Fe,Al)Si-HG, provided that Ca^{2+} concentration is sufficiently low. In complement, Fig. 16 would indicate that magnetite formation due to very low reducing condition would be more likely at 25°C than 80°C even for pH value >11. Moreover, oxidation of iron to Fe^{3+} to form (Fe,Al)Si-HG is thermodynamically favoured in reduced alkaline (OH- rich) cementitious systems with increasing temperature either because the oxygen present in "OH-" is sufficient to promote oxidation (even in reducing conditions) or because of the higher stability of Fe^{3+} vs Fe^{2+} phase (i.e., (Fe,Al)Si-HG) due to their thermodynamic properties.

4.1.5. Open vs closed diffusive system

Among the corrosion studies of carbon-steel in cementitious medium at elevated temperature and in anoxic conditions, only one study reported the formation of (Fe,Al)Si-HG as a corrosion product [26]. In this study, the carbon steel coupon was separated from the cementitious material by a large volume of young cement reservoir solution. Such experimental set-up can be qualified as an open system compared to more tightly closed system as steel embedded in HCP buffer in which diffusion is low. In the present study, the steel rod in direct contact with the reservoir solution can be assimilated to an open system whereas the embedded part can be assimilated to a closed system (depending upon the tightness of the interface).

The question of closed versus open conditions is of interest for the strongly local reducing condition discussed in the previous section since a perfectly tight system prevents any H_2 migration outside the system. The question is also linked to the ingress of elements favouring the formation of (Fe,Al)Si-HG that is controlled by diffusion from both the reservoir solution and the porewater of HCP in direct contact to the steel rod. The simplified modelling of Section 3.2.5 would demonstrate that the more the system is open, the more (Fe,Al)Si-HG is favoured and, on the contrary, the more the system is closed, the more magnetite is favoured. This modelling also indicates that diffusion process could increase the flux of Ca, Al and Si dissolved ions coming from both the reservoir solution and the porewater of the cement matrix located close to the interface. From an experimental point of view, the formation of (Fe,Al)Si-HG by reaction of iron corrosion products with Si, Ca, Al diffusing from the porewater of the HCP is highly likely (Fig. 11). It is probable that reactive Fe^{3+} iron corrosion products had first formed during the cement sub-oxic cement curing phase and then further reacted to form (Fe,Al)Si-HG, but this phenomenon was certainly very limited due to the controlled conditions of the present experiment.

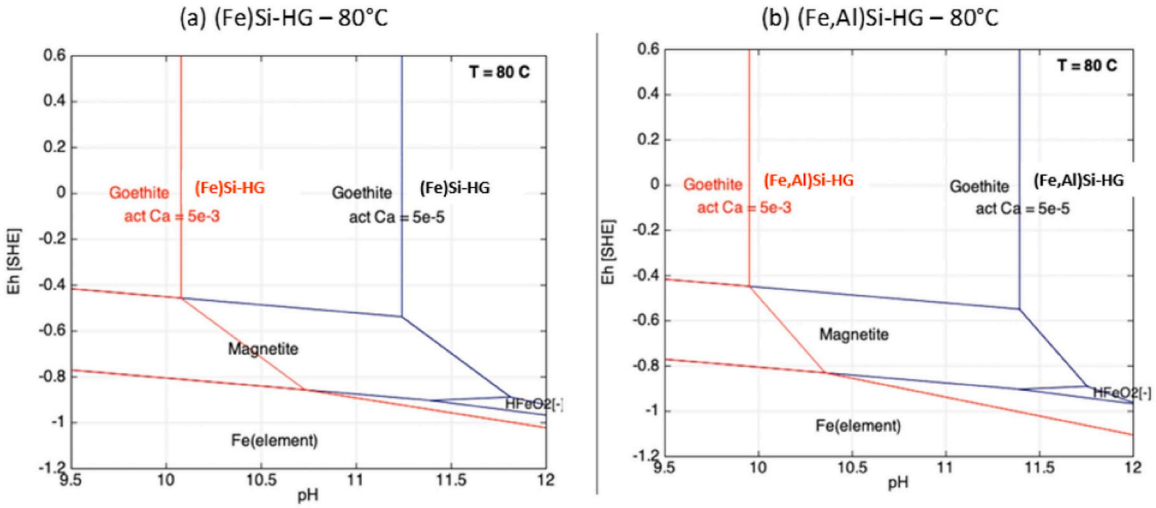

Fig. 17. Simplified Pourbaix diagrams of the (a) Fe – O – Ca – Si system (b) and Fe – O – Ca – Al – Si system calculated with CHESS at 80°C with a sensitivity analysis on the Ca^{2+} activity fixed at 5×10^{-5} (blue lines) or 5×10^{-3} (red lines); activity $Fe^{2+} = 10^{-6}$, activity $Al(OH)_4^- = 5\times10^{-5}$, total $H_4SiO_4 = 10^{-4}$.

Therefore, formation of (Fe,Al)Si-HG from the initial mill-scale layer of the steel elements in the real disposal conditions cannot be discarded. Within these lines, the redissolution of magnetite to form (Fe,Al)Si-HG is modelled in one of the sensitivity cases (Fig. 14-c and d).

4.2. Diffusive barrier effect of the CP layer

In the experiment conducted by Pally et al. (2020) [26], magnetite was observed in the innermost part of the corrosion layer. Formation of nanometric dense layers of magnetite is known to create a passivation film that inhibits the corrosion of steel. The analytical methods used in the present study were not adapted to characterize nanometric layers of oxide, but macroscopic observations suggest that a magnetite layer was formed on the upper parts of the steel rod, where (Fe,Al)Si-HG was not observed. If such magnetite film was also formed in the lower part of the steel rod (i.e., where (Fe,Al)Si-HG was observed), it could then have been destabilized by the presence of other elements coming from the cement to form (Fe,Al)Si-HG.

In the present mock-up tests, formation of (Fe,Al)Si-HG was observed in the first days of the experiment. As previously discussed, the corrosion product layer of (Fe,Al)Si-HG became denser with time and behaved as diffusive barrier that inhibited corrosion mechanism. Consequently, the corrosion rate progressively dropped to values lower than 1 μm/year within less than 100 days of interaction.

Interestingly, some other authors evidenced that Si can play a role in the decrease of corrosion rate of steel in alkaline portlandite saturated solution and anoxic conditions ([11,64,65]). These studies shown that glass cell had an influence on the decrease of the corrosion rate of steel, but neither the Si concentration in solution, nor the nature of the corrosion product were discussed. Silica can sorb in iron oxide/hydroxide phases leading to the conversion of the less stable (more soluble) iron(III) oxides and hydrous oxides, such as ferrihydrite and lepidocrocite, to the more stable forms, goethite and hematite which are Fe^{3+} hydroxide and oxide, respectively [66]. This latter conversion enhances the properties of the steel corrosion layer and protects it against further corrosion. However, the sorption of silica on magnetite is insignificant at high pH [67] and potential modification of the magnetite layer properties due to incorporation of silicon in the system is thus unlikely. Therefore, the Si released from glass dissolution could have reacted with the Ca of the portlandite saturated solution and the Fe dissolved from corrosion to form (Fe,Al)Si-HG in the previously mentioned experiments. In that particular case, the formation of such corrosion product would have a beneficial effect on corrosion rate of the carbon steel.

5. Conclusion

The literature on corrosion of carbon steel in alkaline anaerobic conditions and high temperature in fully saturated conditions representative of nuclear waste disposal conditions is quite exhaustive. Despite the fact that (Fe,Al)Si-hydrogarnet was found to be stable Fe-bearing phase in highly alkaline cement paste and that its formation is predicted by thermodynamic calculations to be stable at the steel concrete interface, only one study reports the formation of such phase as a corrosion product of carbon steel. In the present study, the combined characterization and modelling of the whole system evolution (i.e., cement mineralogy, filling solution chemistry and corrosion evolution) provides new insights on the conditions required to form such (Fe,Al)Si-HG instead of the more common corrosion product magnetite.

Temperature is a key parameter controlling the formation of (Fe,Al)Si-HG, not only for enhancing the kinetics but also for increasing the domain stability of this phase. Temperature increase also promotes the dissolution of cement hydrates that provide elements for (Fe,Al)Si-HG nucleation. As the formation of this phase is controlled by diffusion processes, the geometry of the experimental reactors favoured the transfer of dissolved Ca, Si and Al through the surrounding solution upon the steel surface to initiate precipitation of (Fe,Al)Si-HG. The transformation of iron hydroxide corrosion products into (Fe,Al)Si-HG through diffusion of Ca, Si and Al in the HCP was also emphasized in this study. Ca concentration has been sufficiently high to favour the formation of (Fe,Al)Si-HG against magnetite. In this experiment, Ca release and concentration evolution were predominantly controlled by the pH, portlandite and AFt dissolution. Eventually, highly reducing conditions due to H_2 production from steel anoxic corrosion may promote magnetite against (Fe,Al)Si-HG but were not sufficient in the present study at high temperature, high pH and high Ca concentration.

The formation of (Fe,Al)Si-HG in the high pH cementitious system instead of magnetite challenges the protective properties of the corrosion product layer against corrosion. In the present conditions, the progressive densification of the corrosion product layer allows the formation of a diffusive barrier that hinders corrosion with times even for defective steel surface representative of the material involved in the real disposal conditions.

CRediT authorship contribution statement

Jules Goethals: Conceptualization, Data curation, Formal analysis, Investigation, Methodology, Visualization, Writing – original draft, Writing – review & editing. **Laurent De Windt:** Conceptualization, Data curation,Formal analysis, Investigation, Methodology, Software, Validation, Visualization, Writing – review & editing. **Georges Dan Miron:** Investigation, Software, Validation, Writing – review & editing. **Abdesselam Abdelouas:** Funding acquisition, Investigation, Methodology, Project administration, Resources, Supervision. **Charles Wittebroodt:** Conceptualization, Investigation, Methodology, Validation, Writing – review & editing.

Declaration of Competing Interest

The authors declare the following financial interests/personal relationships which may be considered as potential competing interests: Abdesselam Abdelouas reports financial support was provided by EU Framework Programme for Research and Innovation Euratom. If there are other authors, they declare that they have no known competing financial interests or personal relationships that could have appeared to influence the work reported in this paper.

Data availability

The raw/processed data required to reproduce these findings cannot be shared at this time due to technical or time limitations.

Acknowledgement

This research was funded by the EURAD programme (European Joint Programme on Radioactive Waste Management of the European Union, grant N° 847593) and done within the workpackage ACED (Assessment of Chemical Evolution of ILW and HLW Disposal Cells). The authors would like to thank two anonymous reviewers for their relevant comments as well as Nicolas Stephant from Institut des Matériaux de Nantes (IMN) for his assist with SEM measurements.

Appendix A. Supporting information

Supplementary data associated with this article can be found in the online version at doi:10.1016/j.corsci.2024.112318.

References

[1] D.S. Metlay, Selecting a site for a radioactive waste repository: a historical analysis, Elements 12 (2016) 269–274, https://doi.org/10.2113/gselements.12.4.269.

[2] R.C. Ewing, R.A. Whittleston, B.W.D. Yardley, Geological disposal of nuclear waste: a primer, Elements 12 (2016) 233–237, https://doi.org/10.2113/gselements.12.4.233.

[3] L. de Windt, N.F. Spycher, Reactive transport modeling: a key performance assessment tool for the geologic disposal of nuclear waste, Elements 15 (2019) 99–102, https://doi.org/10.2138/gselements.15.2.99.

[4] S.M. Wickham, M.B. Crawford, D.G. Bennett, Belgian Supercontainer Design for HLW and Spent Fuel Disposal, Eval. Ref. Des. Galson Sci. Ltd, Oakham. (2005).

[5] B. Nős, Needs of countries with longer timescale for deep geological repository implementation, EPJ Nucl. Sci. Technol. 6 (2020) 22, https://doi.org/10.1051/epjn/2019042.

[6] M. Fabian, O. Czompoly, I. Tolnai, L. De Windt, Interactions between C-steel and blended cement in concrete under radwaste repository conditions at 80 °C, Sci. Rep. 13 (2023) 15372, https://doi.org/10.1038/s41598-023-42645-6.

[7] L. De Windt, F. Marsal, J.Ò. Corvisier, D. Pellegrini, Modeling of oxygen gas diffusion and consumption during the oxic transient in a disposal cell of radioactive waste, Appl. Geochem. 41 (2014) 115–127, https://doi.org/10.1016/j.apgeochem.2013.12.005.

[8] D.G. Neeft, E, Weetjens E., Vokal A., Leivo M., Cochepin B., Martin C., Munier I., M. A. Montoya V, Poskas P., Grigaliuniene D., Narkuniene A., García E., Samper J., Montenegro L., Treatment of chemical evolution in National Programmes, D 2.4 of the HORIZON 2020 project EURAD, EC Grant Agreement No: 847593., 2019.

[9] A. Atkinson, N.M. Everitt, R.M. Guppy, Time Dependence of pH in a Cementitious Repository, Materials Research Society, United States, 1989. ⟨http://inis.iaea.org/search/search.aspx?orig_q=RN:21037560⟩.

[10] M. Kaneko, N. Miura, A. Fujiwara, M. Yamamoto, Evaluation of gas generation rate by metal corrosion in the reducing environment, Eng. Report-Radioactive Waste Manag Funding Res. Cent. (RWMC) (2004) 145.

[11] N.A. Senior, T. Martino, N. Diomidis, The anoxic corrosion behaviour of carbon steel in anoxic alkaline environments simulating a Swiss L/ILW repository environment, Mater. Corros. 72 (2021) 131–140, https://doi.org/10.1002/maco.202011780.

[12] N. Senior, T. Martino, N. Diomidis, R. Gaggiano, The anoxic corrosion of mild steel in a cementitious repository environment, Mater. Corros. (2023), https://doi.org/10.1002/maco.202313765.

[13] N.R. Smart, Corrosion behavior of carbon steel radioactive waste packages: a summary review of Swedish and U.K. Research, Corrosion 65 (2009) 195–212, https://doi.org/10.5006/1.3319128.

[14] N.R. Smart, A.P. Rance, D.J. Nixon, P.A.H. Fennell, B. Reddy, B. Kursten, Summary of studies on the anaerobic corrosion of carbon steel in alkaline media in support of the Belgian supercontainer concept, Corros. Eng. Sci. Technol. 52 (2017) 217–226, https://doi.org/10.1080/1478422X.2017.1356981.

[15] L. Chomat, E. Amblard, J. Varlet, C. Blanc, Passive corrosion of steel reinforcement in blended cement-based material in Corrosion Engineering, Science and Technology Passive corrosion of steel reinforcement in blended cement-based material in the context of nuclear waste disposal, Corros. Eng. Sci. Technol. (2017) 148–154, https://doi.org/10.1080/1478422X.2017.1300378.

[16] B. Kursten, F. Druyts, L. Areias, Y. van Ingelgem, D. De Wilde, G. Nieubourg, G. S. Duffó, C. Bataillon, Preliminary results of corrosion monitoring studies of carbon steel overpack exposed to supercontainer concrete buffer, Corros. Eng. Sci. Technol. 49 (2014) 485–491, https://doi.org/10.1179/1743278214Y.0000000216.

[17] C. Padovani, F. King, C. Lilja, D. Féron, S. Necib, D. Crusset, V. Deydier, R. Gaggiano, T. Ahn, P.G. Keech, D.D. Macdonald, H. Asano, D.S. Hall, H. Hänninen, D. Engelberg, J.J. Noël, D.W. Shoesmith, F. King, C. Lilja, D. Féron, S. Necib, D. Crusset, V. Deydier, The Corrosion Behaviour of Candidate Container Materials for the Disposal of High-level Waste and Spent Fuel – A Summary of the State of the Art and Opportunities for Synergies in Future R & D 2782 (2017), https://doi.org/10.1080/1478422X.2017.1356973.

[18] E. Garcia, J. Torres, N. Rebolledo, R. Arrabal, J. Sanchez, Corrosion of steel rebars in anoxic environments. Part i: electrochemical measurements, Materials 14 (2021) 1–15, https://doi.org/10.3390/ma14102491.

[19] N. Senior, T. Martino, N. Diomidis, R. Gaggiano, W. Binns, P. Keech, The measurement of ultra low uniform corrosion rates, Corros. Sci. 176 (2020) 108913, https://doi.org/10.1016/j.corsci.2020.108913.

[20] B. Kursten, D.D. Macdonald, N.R. Smart, R. Gaggiano, Corrosion issues of carbon steel radioactive waste packages exposed to cementitious materials with respect to the Belgian supercontainer concept, Corros. Eng. Sci. Technol. 52 (2017) 11–16, https://doi.org/10.1080/1478422X.2017.1292345.

[21] B. Kursten, F. Druyts, D.D. Macdonald, N.R. Smart, R. Gens, L. Wang, E. Weetjens, J. Govaerts, Review of corrosion studies of metallic barrier in geological disposal conditions with respect to Belgian Supercontainer concept, Corros. Eng. Sci. Technol. 46 (2011) 91–97, https://doi.org/10.1179/1743278210Y.0000000022.

[22] V. L'Hostis, E. Amblard, C. Blanc, F. Miserque, C. Paris, L. Bellot-Gurlet, Passive corrosion of steel in concrete in context of nuclear waste disposal, Corros. Eng. Sci. Technol. 46 (2011) 177–181, https://doi.org/10.1179/1743278210Y.0000000013.

[23] L. Chomat, V. L'Hostis, E. Amblard, L. Bellot-Gurlet, Long term study of passive corrosion of steel rebars in Portland mortar in context of nuclear waste disposal, Corros. Eng. Sci. Technol. 49 (2014) 467–472, https://doi.org/10.1179/1743278214Y.0000000201.

[24] L. De Windt, G.D. Miron, M. Fabian, J. Goethals, C. Wittebroodt, EURAD Deliverable 2.8: First rEsults on the Thermodynamic Databases and Reactive Transport Models for Steel-cement Interfaces at High Temperature, (2020). ⟨https://hal-mines-paristech.archives-ouvertes.fr/hal-03107880⟩.

[25] E. Wieland, G.D. Miron, B. Ma, G. Geng, B. Lothenbach, Speciation of iron(II/III) at the iron-cement interface: a review, Mater. Struct. Constr. 56 (2023), https://doi.org/10.1617/s11527-023-02115-x.

[26] D. Pally, P. Le Bescop, M.L. Schlegel, F. Miserque, L. Chomat, D. Neff, V. L'Hostis, Corrosion behavior of iron plates in cementitious solution at 80 °C in anaerobic conditions, Corros. Sci. 170 (2020) 108650, https://doi.org/10.1016/j.corsci.2020.108650.

[27] J. Goethals, L. De Windt, C. Wittebroodt, A. Abdelouas, X. de la Bernardie, Y. Morizet, B. Zajec, V. Detilleux, Interaction between carbon steel and low-pH bentonitic cement grout in anoxic, high temperature (80 °C) and spatially heterogeneous conditions, Corros. Sci. 211 (2023) 110852, https://doi.org/10.1016/j.corsci.2022.110852.

[28] P. Lalan, A. Dauzères, L. De Windt, D. Bartier, J. Sammaljärvi, J.D. Barnichon, I. Techer, V. Detilleux, Impact of a 70 °c temperature on an ordinary Portland cement paste/claystone interface: an in situ experiment, Cem. Concr. Res. 83 (2016) 164–178, https://doi.org/10.1016/j.cemconres.2016.02.001.

[29] P. Lalan, A. Dauzères, L. De Windt, J. Sammaljärvi, D. Bartier, I. Techer, V. Detilleux, M. Siitari-Kauppi, Mineralogical and microstructural evolution of Portland cement paste/argillite interfaces at 70 °C – Considerations for diffusion and porosity properties, Cem. Concr. Res. 115 (2019) 414–425, https://doi.org/10.1016/j.cemconres.2018.09.018.

[30] B. Lothenbach, G. Le Saout, E. Gallucci, K. Scrivener, Influence of limestone on the hydration of Portland cements, Cem. Concr. Res. 38 (2008) 848–860, https://doi.org/10.1016/j.cemconres.2008.01.002.

[31] B.Z. Dilnesa, E. Wieland, B. Lothenbach, R. Dähn, K.L. Scrivener, Fe-containing phases in hydrated cements, Cem. Concr. Res. 58 (2014) 45–55, https://doi.org/10.1016/j.cemconres.2013.12.012.

[32] G.D. Miron, D.A. Kulik, B. Lothenbach, Porewater compositions of Portland cement with and without silica fume calculated using the fine-tuned CASH+NK solid solution model, Mater. Struct. Constr. 55 (2022) 1–13, https://doi.org/10.1617/s11527-022-02045-0.

[33] B. Lothenbach, F. Winnefeld, Thermodynamic modelling of the hydration of Portland cement, Cem. Concr. Res. 36 (2006) 209–226, https://doi.org/10.1016/j.cemconres.2005.03.001.

[34] ASTM, Standard Practice for Preparing, Cleaning, and Evaluating Corrosion Test Specimens., Philadelphia, United States, 2011.

[35] J. van der Lee, L. De Windt, V. Lagneau, P. Goblet, Module-oriented modeling of reactive transport with HYTEC, Comput. Geosci. 29 (2003) 265–275, https://doi.org/10.1016/S0098-3004(03)00004-9.

[36] P. Blanc, P. Vieillard, H. Gailhanou, S. Gaboreau, N. Marty, F. Claret, B. Madé, E. Giffaut, ThermoChimie database developments in the framework of cement/clay interactions, Appl. Geochem. 55 (2015) 95–107, https://doi.org/10.1016/j.apgeochem.2014.12.006.

[37] B.Z. Dilnesa, B. Lothenbach, G. Renaudin, A. Wichser, D. Kulik, Synthesis and characterization of hydrogarnet Ca3(Al xFe1 - X)2(SiO4)y(OH) 4(3 - y), Cem. Concr. Res. 59 (2014) 96–111, https://doi.org/10.1016/j.cemconres.2014.02.001.

[38] B. Lothenbach, T. Matschei, G. Möschner, F.P. Glasser, Thermodynamic modelling of the effect of temperature on the hydration and porosity of Portland cement, Cem. Concr. Res. 38 (2008) 1–18, https://doi.org/10.1016/j.cemconres.2007.08.017.

[39] R. Barbarulo, H. Peycelon, S. Leclercq, Chemical equilibria between C-S-H and ettringite, at 20 and 85 °C, Cem. Concr. Res. 37 (2007) 1176–1181, https://doi.org/10.1016/j.cemconres.2007.04.013.

[40] K. Kyritsis, N. Meller, C. Hall, Chemistry and morphology of hydrogarnets formed in cement-based CASH hydroceramics cured at 200° to 350°C, J. Am. Ceram. Soc. 92 (2009) 1105–1111, https://doi.org/10.1111/j.1551-2916.2009.02958.x.

[41] E. Passaglia, R. Rinaldi, A new nomenclature for the hydrogrossular group of minerals, Bull. Minér. 107 (1984) 605–618.

[42] M. Shafikhani, S.E. Chidiac, Quantification of concrete chloride diffusion coefficient – a critical review, Cem. Concr. Compos. 99 (2019) 225–250, https://doi.org/10.1016/j.cemconcomp.2019.03.011.

[43] J. Peña, E. Torres, M.J. Turrero, A. Escribano, P.L. Martín, Kinetic modelling of the attenuation of carbon steel canister corrosion due to diffusive transport through corrosion product layers, Corros. Sci. 50 (2008) 2197–2204, https://doi.org/10.1016/j.corsci.2008.06.004.

[44] S. Hillier, D.G. Lumsdon, R. Brydson, E. Paterson, Hydrogarnet: A host phase for Cr (VI) in chromite ore processing residue (COPR) and other high pH wastes, Environ. Sci. Technol. 41 (2007) 1921–1927, https://doi.org/10.1021/es0621997.

[45] R.S. Gollop, H.F.W. Taylor, Microstructural and microanalytical studies of sulfate attack. II. Sulfate-resisting Portland cement: ferrite composition and hydration chemistry, Cem. Concr. Res. 24 (1994) 1347–1358, https://doi.org/10.1016/0008-8846(94)90120-1.

[46] M. Vespa, E. Wieland, R. Dähn, B. Lothenbach, Identification of the thermodynamically stable Fe-containing phase in aged cement pastes, J. Am. Ceram. Soc. 98 (2015) 2286–2294, https://doi.org/10.1111/jace.13542.

[47] G. Le Saout, E. Lécolier, A. Rivereau, H. Zanni, Chemical structure of cement aged at normal and elevated temperatures and pressures: part I. Class G oilwell cement, Cem. Concr. Res. 36 (2006) 71–78, https://doi.org/10.1016/j.cemconres.2004.09.018.

[48] N. Neuville, E. Lecolier, G. Aouad, A. Rivereau, D. Damidot, Effect of curing conditions on oilwell cement paste behaviour during leaching, Exp. Model. Approaches, Comptes Rendus - Chim. 12 (2009) 511–520, https://doi.org/10.1016/j.crci.2008.06.006.

[49] M.S. Morsy, Effect of temperature on hydration kinetics and stability of hydration phases of metakaolin-lime sludge-silica fume system, Ceram. - Silik. 49 (2005) 237–241.

[50] D.P. Prentice, B. Walkley, S.A. Bernal, M. Bankhead, M. Hayes, J.L. Provis, Thermodynamic modelling of BFS-PC cements under temperature conditions relevant to the geological disposal of nuclear wastes, Cem. Concr. Res. 119 (2019) 21–35, https://doi.org/10.1016/j.cemconres.2019.02.005.
[51] N.C. Collier, N.B. Milestone, J. Hill, I.H. Godfrey, The disposal of radioactive ferric floc, Waste Manag 26 (2006) 769–775, https://doi.org/10.1016/j.wasman.2006.01.031.
[52] N.C. Collier, N.B. Milestone, J. Hill, I.H. Godfrey, Immobilisation of Fe floc: Part 2, encapsulation of floc in composite cement, J. Nucl. Mater. 393 (2009) 92–101, https://doi.org/10.1016/j.jnucmat.2009.05.010.
[53] S. Caré, Effect of temperature on porosity and on chloride diffusion in cement pastes, Constr. Build. Mater. 22 (2008) 1560–1573, https://doi.org/10.1016/j.conbuildmat.2007.03.018.
[54] P.W. Brown, D. Shi, A model for the variations in solution chemistry during tricalcium silicate hydration, Adv. Cem. Res. 4 (1991) 17–27, https://doi.org/10.1680/adcr.1991.4.1.17.
[55] E.P. Flint, L.S. Wells, Relationship of the garnet-hydrogarnet series to the sulfate resistance of portland cements, J. Res. Natl. Bur. Stand. 27 (1934) (1941) 171, https://doi.org/10.6028/jres.027.007.
[56] B. Li, X. Lu, B. Huo, Y. Du, Y. Liu, Y. Cheng, Z. Liu, The early age hydration products and mechanical properties of cement paste with steel slag powder as additive under steam curing conditions, Buildings 13 (2023), https://doi.org/10.3390/buildings13092192.
[57] M.L. Schlegel, F. Martin, M. Fenart, C. Blanc, J. Varlet, E. Foy, D. Prêt, N. Trcera, Corrosion at the carbon steel-clay compact interface at 90°C: insight into short- and long-term corrosion aspects, Corros. Sci. 152 (2019) 31–44, https://doi.org/10.1016/j.corsci.2019.01.027.
[58] K.L. Scrivener, A. Capmas, Calcium aluminate cements, in: P. Hewlett (Ed.), Lea's Chem. Cem. Concr., fourth ed, Butterworth-Heinemann, Oxford, 1998, pp. 713–782, https://doi.org/10.1016/B978-075066256-7/50025-4.
[59] M.U. Okoronkwo, F.P. Glasser, Compatibility of hydrogarnet, Ca3Al2(SiO4)x(OH)4(3 -X), with sulfate and carbonate-bearing cement phases: 5-85 °c, Cem. Concr. Res. 83 (2016) 86–96, https://doi.org/10.1016/j.cemconres.2016.01.013.
[60] B. Dilnesa, B. Lothenbach, G. Renaudin, A. Wichser, E. Wieland, H. Jennings, Stability of monosulfate in the presence of iron, J. Am. Ceram. Soc. 95 (2012), https://doi.org/10.1111/j.1551-2916.2012.05335.x.
[61] G. Möschner, B. Lothenbach, F. Winnefeld, A. Ulrich, R. Figi, R. Kretzschmar, Solid solution between Al-ettringite and Fe-ettringite (Ca6[Al1 - xFex(OH)6]2(SO4)3·26H2O), Cem. Concr. Res. 39 (2009) 482–489, https://doi.org/10.1016/j.cemconres.2009.03.001.
[62] A. Mancini, E. Wieland, G. Geng, B. Lothenbach, B. Wehrli, R. Dähn, Fe(II) interaction with cement phases: method development, wet chemical studies and X-ray absorption spectroscopy, J. Colloid Interface Sci. 588 (2021) 692–704, https://doi.org/10.1016/j.jcis.2020.11.085.
[63] A. Mancini, E. Wieland, G. Geng, R. Dähn, J. Skibsted, B. Wehrli, B. Lothenbach, Fe (III) uptake by calcium silicate hydrates, Appl. Geochem. 113 (2020), https://doi.org/10.1016/j.apgeochem.2019.104460.
[64] C. Naish. Blackwood, D.J. Thomas, M.I. Rance, AP, The Anaerobic Corrosion of Carbon Steel and Stainless Steel, Report AEAT/R/ENV/0224, U.K., 2001.
[65] N. Smart, Blackwood D.J., Marsh G.P., Naish C.C., O'Brien T.M., Rance A.P., Thomas MI, The Anaerobic Corrosion of Carbon and Stainless Steels in Simulated Cementitious Repository Environments: a summary review of Nirex Research, Report AEAT/ERRA-0313, U.K., 2004.
[66] P. Taylor, Interactions of silica with iron oxides: Effects on oxide transformations and sorption properties, Canada, 1995. ⟨http://inis.iaea.org/search/search.aspx?orig_q=RN:27012842⟩.
[67] V. Philippini, A. Naveau, H. Catalette, S. Leclercq, Sorption of silicon on magnetite and other corrosion products of iron, J. Nucl. Mater. 348 (2006) 60–69, https://doi.org/10.1016/j.jnucmat.2005.09.002.